Volatile-rich magmas distributed through the upper crust in the Main Ethiopian Rift

Fiona Iddon & Marie Edmonds*

Department of Earth Sciences, University of Cambridge

*Corresponding author: Marie Edmonds (marie.edmonds@esc.cam.ac.uk)

Key Points:

- Alkali basalts are stored both on- and off-axis at depths >15 km in the crust, on-axis peralkaline rhyolites are stored at between ~4-8 km depth.
- Saturation of mafic magmas in a sulfide and exsolved volatile phase in the Daly Gap promotes buoyancy and rise of magmas to shallower reservoirs, where protracted fractional crystallisation and degassing occurs.
- Caldera-forming, explosive eruptions in the MER may give rise to large emissions of SO_2 and halogens, which may have significant environmental impacts.
- A significant pre-eruptive exsolved volatile phase should be considered when interpreting geophysical monitoring data to avoid producing underestimates of intruded magma volumes.

Abstract

Understanding magma storage and differentiation in the East African Rift underpins our understanding of volcanism in continental rift settings. Here we present the geochemistry of melt inclusions erupted in Main Ethiopian Rift transitional basalts, trachytes and peralkaline rhyolites, produced by fractional crystallisation. Basalts stored on- and off-axis are saturated in an exsolved volatile phase at up to 18 km, in the upper crust. Much of the CO_2 outgassed from the magmas is likely lost through diffuse degassing. Observed CO_2 fluxes require the intrusion of up to 0.14 km^3 of basalt beneath the rift each year. On-axis peralkaline rhyolites

are stored shallowly, at ~4-8 km depth. In the Daly Gap, magmas saturate in sulfide and an exsolved volatile phase, which promotes magma rise to shallower levels in the crust. Here, magmas undergo further protracted fractional crystallisation and degassing, leading to the formation of a substantial exsolved volatile phase, which may accumulate in a gas-rich cap. The exsolved volatile phase is rich in sulfur and halogens: their projected loadings into the atmosphere during explosive peralkaline eruptions in the MER are predicted to be substantially higher than their metaluminous counterparts in other settings. The high fraction of exsolved volatiles in the stored magmas enhances their compressibility and must be considered when interpreting ground displacements thought to be caused by magma intrusion at depth, otherwise intruding volumes will be underestimated. Pockets of exsolved volatiles may be present at the roof zones of magma reservoirs, which may be resolvable using geophysical techniques.

Index Terms

1009, 1043, 8430, 8488, 8485

Keywords

Peralkaline, Main Ethiopian Rift, melt inclusions, magmatic volatiles, volcanic degassing

1. Introduction

An important goal of many studies of volcano-magmatic systems is to extract a record of pre-eruptive melt chemistry and use it to assess magma differentiation and the conditions of magma storage and processing in the crust. Whole-rock compositions in many cases do not represent melt compositions; they encompass not only the carrier liquid, but also the crystals the magma carries. There is strong evidence that crystals in volcanic rocks are frequently not in equilibrium with their carrier melts, having been scavenged from different magmas [*Davidson and Tepley*, 1997; *Tepley et al.*, 2000], crystalline mushes [*Bachmann et al.*, 2002; *Cooper and Kent*, 2014], or even wall-rock [*Taylor Jr*, 1980]. Isolation of pockets of melt trapped inside growing crystals after entrapment in relatively incompressible crystal hosts may allow the preservation of early-stage melts, isolating them from subsequent processing related to storage, ascent and eruption [*Kent*, 2008; *Lowenstern*, 1995]. If used carefully, with

consideration given to post-entrapment modification [*Moore et al.*, 2015; *Steele-Macinnis et al.*, 2011], primary melt inclusion trace and volatile element concentrations may be used to examine differentiation processes, including mixing and degassing, during the evolution of magmas [*Métrich et al.*, 2001; *Sobolev*, 1996].

Melt inclusion studies of peralkaline volcanic rocks are scarce in the literature [*Barclay et al.*, 1996; *Gioncada and Landi*, 2010; *Lanzo et al.*, 2013; *Macdonald et al.*, 2012; *Neave et al.*, 2012] and consequently, we have only a very limited picture of differentiation processes, conditions of pre-eruptive storage and the volatile budget of peralkaline volcanic systems. Peralkaline melts have an excess of alkalis with respect to aluminium (molar $(Na_2O+K_2O)/Al_2O_3>1$) [*Shand*, 1927]. The high alkali contents of the melts enhance solubility of volatiles including CO_2, H_2O, F and Cl [*Di Matteo et al.*, 2004; *Scaillet and Macdonald*, 2006; *Shishkina et al.*, 2014; *Webster et al.*, 2015]. Peralkaline eruptions are predicted to release larger masses of sulfur dioxide gas into the atmosphere than their metaluminous and peraluminous counterparts owing to the combination of high sulfur concentrations at sulfide saturation (which minimises sulfide precipitation) and high fluid/melt partition coefficients (>200) at typical magma reservoir pressures and temperatures [*Scaillet and Macdonald*, 2006]. The systematics of halogen behaviour in peralkaline melts is complex [*Webster et al.*, 2015] and may involve saturation of a low density vapour as well as a brine phase in the shallower parts of the crustal storage system, whereby the melt Cl content becomes buffered at a fixed value, which may be used to estimate magma storage depths [*Balcone-Boissard et al.*, 2016].

Understanding the volatile budget of volcanic systems in the Main Ethiopian Rift (MER) is not only important for understanding the liquid line of descent, the outgassing potential for eruptions and the behaviour of the exsolved volatile phase in the crust, but also has implications for the interpretation of geophysical monitoring signals captured there in recent years and for estimating magma budgets. Interferometric Synthetic Aperture Radar (InSAR) observations of ground deformation suggest magmatic unrest at a number of MER calderas [*Biggs et al.*, 2011; *Hutchison et al.*, 2016a; *Lloyd et al.*, 2018], however, the compressibility of any exsolved volatile phase is an important control on ground displacements and must be understood to infer magma volumes at depth [*Biggs et al.*, 2014a; *McCormick Kilbride et al.*,

2016]. Significant diffuse soil CO_2 degassing has also been observed along the MER and East African Rift System (EARS) [*Hunt et al.*, 2017; *Hutchison et al.*, 2015; *Lee et al.*, 2016], testifying to the presence of unerupted magma bodies at depth. Understanding the primary melt CO_2 contents of the basalts at depth may allow estimates of magma supply rate beneath the rift to be developed.

Here, we present major, trace, and volatile element data for melt inclusions from the eruptive products of five different volcanic sites: Corbetti, Kone, Fentale and Aluto central volcanoes, and the Butajira volcanic field (BVF) (**figure 1**). Fractional crystallisation models are constructed based on trace element mineral-melt partitioning data, using Principal Component Analysis (PCA) of the liquid line of descent to constrain the crystallising mineral assemblages. These models are then used, in tandem with volatile saturation models, to track volatile behavior through the evolution of the MER melts. Depths of magma storage and magma fluxes are estimated based on the abundance of H_2O and CO_2 in the melt inclusions and compared with barometry using clinopyroxene and melt compositions, whilst estimates of the mass fraction of exsolved volatiles are used to approximate the quantity of sulfur released during past eruptions. Inferences are made about the impact of an exsolved volatile phase on magma compressibility and its potential effects on ground displacements monitored at the surface.

2 Geological Setting

The MER is the northern-most portion of the EARS. Extending for ~1000 km in a NNE-SSW direction from the Afar to the Turkana depression, it separates the Nubian and Somalian plates (**figure 1**) [*Mohr*, 1983; *Woldegabriel et al.*, 1990]. The MER is currently undergoing active east-west extension of ~5 mm yr^{-1} [*Saria et al.*, 2014], with recent geodetic data showing that 80% of the current strain is accommodated on the Wonji Fault Belt (WFB) [*Bilham et al.*, 1999]. The WFB is a group of short N-NE trending *en echelon* faults that lie within a ~15 km wide axial zone in the MER (**figure 1**) [*Agostini et al.*, 2011; *Keir et al.*, 2006]. Pleistocene and Holocene volcanism has been focused within tectono-magmatic segments along the rift that are co-located with the WFB [*Abebe et al.*, 2007; *Corti*, 2009; *Fontijn et al.*, 2018].

Quaternary to recent MER volcanism is typified by peralkaline axis-central caldera systems that are located at the ends of the volcanic segments (**figure 1**) [*Beutel et al.*, 2010; *Keranen et al.*, 2004]. These areas are under reduced extensional stresses and may involve colder crust [*Ebinger et al.*, 2008]. Such conditions might hinder magma ascent and facilitate longer residence times and fractionation [*Hutchison et al.*, 2015; *Peccerillo et al.*, 2003]. Pumice samples were selected from four different caldera systems along the length of the MER: Corbetti, Aluto, Kone, and Fentale (**figure 1**). Following large (VEI > 5) caldera-forming eruptions at ~300 ka [*Hutchison et al.*, 2016a], the different silicic centres have displayed variable post-caldera eruption styles [*Fontijn et al.*, 2018]. Some volcanoes have erupted predominately rhyolite lava flows (e.g. Fentale), whilst others have had multiple sub-Plinian eruptions (e.g. Corbetti and Aluto) [*Fontijn et al.*, 2018]. Both syn- and post-caldera pumice samples have been investigated. The most recent deposits are the products of basaltic volcanism, with eruptions continuing at sites such as Kone and Fentale into historic times (the last eruption of both volcanoes was in 1820) [*Harris*, 1844]. Basaltic scoria cones and associated lava flows are arranged linearly along faults and extensional fractures [*Hunt et al.*, 2020; *Rooney et al.*, 2011]; the stress conditions located at the fault tips are thought to promote magma ascent and cone eruptions.

Recent mafic volcanism has also occurred near the western escarpment of the rift along the Silti-Debre Zeit Fault Zone (SDFZ; **figure 1**) [*Chernet and Hart*, 1999; *Rooney et al.*, 2005; *Woldegabriel et al.*, 1990]. Extending from 6.5°N to 9°N [*Rooney et al.*, 2005], the SDFZ is a 2-5 km wide belt dominated by off-axis volcanic fields of basaltic scoria cones and associated lava flows [*Woldegabriel et al.*, 1990]. The BVF mafic volcanism in the region has been dated at 0.13 Ma [*Woldegabriel et al.*, 1990] and 0.11 Ma [*Chernet et al.*, 1998], in line with the Wonji Basalts.

3 Methods

The Corbetti pumice samples used in this study were collected by Raffaella Fusillo between 2012 and 2014 [*Fusillo*, 2018]. The Aluto and Kone samples were collected by Karen Fontijn and Keri McNamara in November 2015, and by William Hutchison [*Hutchison*, 2015] and Michael Rampey [*Rampey*, 2005]. The Aluto samples comprised 1 post-caldera basaltic scoria sample, 1 syn-caldera trachyandesite enclave, 2 syn-caldera welded ignimbrites, 3

post-caldera rhyolite lavas (glassy selvages) and 4 post-caldera pumices. Additional Kone samples and Fentale samples were collected by Fiona Iddon, Jonathan Hunt, and Abate Assen in October 2017, which comprised 7 post-caldera basaltic scoria samples, 7 syn-caldera pumice samples, 1 syn-caldera welded ignimbrite and 2 pre-caldera glassy, silicic lava samples. Tephra samples from 6 scoria cones in the Butajira Volcanic Field (hereafter BVF) were collected by Iddon and Juliane Hubert during a sampling campaign in 2017. Additional detail on the samples and their context is given in the **Supplementary Material**. Olivines and quartz were hand-picked from crushed material and mounted on glass slides. Crystals were manually polished to expose melt inclusions, before the crystals were extracted and mounted into epoxy blocks and polished down to a fine grade using 9 μm, 6 μm, 3 μm, 1 μm and 0.25 μm grade diamond paste.

Melt inclusions were screened at two stages during their preparation. During initial polishing of the individual host minerals the inclusions were examined via reflected light microscopy. Those selected for final mounting (those showing no evidence of cracking or daughter crystals) were examined using the Quanta-650F Scanning Electron Microscope (SEM) at the University of Cambridge. BSE images and maps of the blocks were taken under low vacuum (to avoid having to carbon coat them and risk contamination prior to SIMS analysis of CO_2). Melt inclusions that showed visible evidence of cracks, shrinkage bubbles, or post-entrapment crystallisation were avoided.

Melt inclusions and adherent matrix glasses were analysed by Secondary Ion Mass Spectrometry (SIMS) using the Cameca ims-4f ion probe at NERC microanalytical facility at the University of Edinburgh for trace and volatile elements. Major elements, Cl and F were analysed by Electron Probe Micro Analysis (EPMA) using the a Cameca SX-100 Electron Probe Micro-Analyser at the University of Cambridge. Detailed descriptions of these methods, standards used [*Shishkina et al.*, 2010], and the associated errors are given in the **Supplementary Materials**.

Corrections for post-entrapment crystallization (PEC) were made for the olivine-hosted melt inclusions. Host olivine compositions were measured using EPMA on spots within 40 μm of the inclusion edge. A combined correction was applied for Fe-loss and PEC [*Danyushevsky*

and Plechov, 2011]. The iterative correction scheme requires knowledge of melt inclusion geochemistry, including H_2O content, host olivine Fo content, oxidation state of the melt, and the initial melt inclusion FeO content at the time of entrapment, taken as average matrix glass FeO [*Putirka*, 2005], resulting in corrections of <5%; for full details see **Supplementary Material**. When the major element composition of the quartz-hosted inclusions were recalculated on an anhydrous basis, most do not show any depletion of silica or relative enrichment of other major elements (see **Supplementary Material**) that would reflect post-entrapment crystallisation of quartz.

4 Results

4.1 Melt inclusion and matrix glass major element compositions

Olivine compositions range from 58 to 77 mol% forsterite (see **Supplementary Data**). The majority of host olivine cores (compositions provided in **Supplementary Material**) are in equilibrium with their host melts (matrix glasses) [*Roeder and Emslie*, 1970], but there is some variability in olivine forsterite contents for a given melt Mg# (**see Supplementary Material figure S4**). Melt inclusion and matrix glass compositions are provided in **Supplementary Material** and **figure 2**. The melt inclusion compositions are basaltic, trachy-basaltic, trachytic and rhyolitic and display a distinct Daly Gap at between ~52 and 64 wt.% SiO_2 (**figure 2a**). All of the evolved samples are peralkaline, with most classified as pantellerites based on their high FeO concentrations (**figure 2b**) [*Macdonald*, 1974]. The Corbetti inclusions sit on the border with comendite owing to their lower FeO and high Al_2O_3 contents. The olivine-hosted melt inclusions are basalts and trachybasalts that have a transitional composition (**figure 2a**).

With increasing SiO_2 content of the glasses there is a corresponding increase in alkalis and a decrease in ferromagnesian, Ti, Ca, and P oxides (**figure 2**). K_2O increases smoothly and largely linearly with SiO_2 content, whilst Al_2O_3 contents rise to ~20 wt.% before falling to <10 wt.% in the pantellerite samples (**figure 2d, j**). Na_2O displays considerable variation (2.0–7.0 wt.%) across the basaltic to pantellerite glasses (**figure 2i**). BVF matrix glasses and inclusions contain up to ~15 wt.% FeO, in contrast to Kone olivine-hosted melt inclusions, which contain between ~5 and 10 wt.% FeO contents (**figure 2e**). There appears to be little variation in FeO content between the olivine-hosted and quartz-hosted melt inclusions. BVF

glasses have particularly low MgO contents at <4.5 wt.%; additionally, they have low Al_2O_3 contents, at <15 wt.%, and elevated TiO_2 and P_2O_5 contents, ranging to >4 wt.% and >1.5 wt.%, respectively (**figure 2**). The quartz-hosted melt inclusions show considerable compositional spread; however, the Corbetti samples are noteworthy for their low FeO and MnO contents, <5 and 0.2 wt.% respectively (**figure 2f**).

4.2 Melt inclusion and matrix glass trace element compositions

Melt inclusion and matrix glass compositions are provided in **Supplementary Material**. The co-variation of selected trace elements with Zr, which is highly incompatible in peralkaline melts, is shown in **figure 3**. The Kone and BVF mafic melt inclusion Zr contents overlap, whilst the matrix glasses show a slightly higher Zr content consistent with a greater degree of evolution. The Daly Gap is evident in the trace element compositions: melt inclusions with Zr contents between ~230 and ~600 ppm are sparse (**figure 3**). Compatible elements show a negative correlation with Zr: e.g. Sr increases up to ~750 ppm before an inflection point at a Zr content of ~200 ppm, when feldspar begins to crystallise (**figure 3f**). Incompatible elements (Rb and the REE) show approximately linear positive trends (**figure 3a, c-e, g, h, j-q**). Olivine-hosted melt inclusions from BVF and quartz-hosted melt inclusions from Fentale show a slight enrichment in Y (**figure 3m**) and the HREE (**figure 3n, o, and q**) over olivine-hosted melt inclusions from Kone and quartz-hosted melt inclusions from the other silicic centres. Aluto and Fentale melt inclusions show a slight enrichment in the MREE (**figure 3j-l**) relative to the quartz-hosted melt inclusions from the other silicic centres. Quartz-hosted melt inclusions and matrix glasses from Kone show a large spread in Rb contents (**figure 3a)**. The Rb enrichment observed in the Kone samples, as compared to the other silicic centres, is unlikely to be related to crustal contamination as Rb/Nb ratios are generally lower than that of the Precambrian crustal rocks [*Peccerillo et al.*, 1998] (**figure 3r**). Ba (**figure 3b**) and Eu (**figure 3i**) contents show scatter when plotted against Zr, particularly for the quartz-hosted melt inclusions: melt inclusions contain 12–1200 ppm for Ba, 1.5-15 ppm for Eu. The Fentale samples that show high Ba and Eu concentrations do not show any notable enrichment or depletion in Rb concentrations relative to quartz-hosted melt inclusions from the other silicic centres (**figure 3a**).

4.3 Melt inclusion and matrix glass volatile concentrations

Melt inclusion and matrix glass volatile compositions are provided in **Supplementary Material**. Melt inclusion H_2O contents range from ~2 wt.% to <0.5 wt.% in the BVF and the Kone olivine-hosted melt inclusions (**figure 4a**). There is a large spread in the H_2O contents of the quartz-hosted melt inclusions, from <2 to 8 wt.% H_2O (**figure 4a**). Fentale and Corbetti melt inclusions contain H_2O contents up to 4 wt.%. Matrix glasses typically contain <0.05 wt% H_2O.

Olivine-hosted melt inclusion CO_2 contents range from <500 ppm to >3000 ppm over a Zr range of 55 ppm to 220 ppm in the mafic samples (**figure 4c**). BVF melt inclusions show slightly higher CO_2 contents of up to 5000 ppm (**figure 4c**). The quartz-hosted melt inclusions contain between ~100 and ~300 ppm CO_2 (**figure 4c**). Matrix glasses have very low CO_2 contents, below detection limits (**figure 4c**). Melt halogen contents increase with Zr concentration: Cl and F increase from 130 to ~1000 ppm and <900 to ~1500 ppm respectively as Zr increases from 55 to 220 ppm (**figure 4e and f**). There is a decrease in the gradient on the halogen vs Zr plots in the quartz-hosted melt inclusions relative to the olivine-hosted melt inclusions. Melt Cl contents reach up to 4000 ppm in the most evolved samples, whilst F contents reach up to 7000 ppm, though the dataset shows some spread (**figure 4e and f**). Corbetti samples show particularly low halogen contents, with Cl <1900 ppm and F <2700 ppm; Fentale samples show low F contents (<3750 ppm) (**figure 4e and f**).

Olivine-hosted melt inclusions show a positive correlation between melt sulfur contents and Zr, increasing from ~2000 to ~3000 ppm S with increasing Zr (**figure 4d**). The quartz-hosted melt inclusions contain up to ~600 ppm S and S does not correlate with Zr (**figure 4d**). In contrast to the halogens and sulfur, Li and B increase linearly with melt Zr contents, reaching up to ~100 ppm and ~20 ppm respectively (**figure 4g and h**). There is some spread in the Li dataset, with the most evolved samples showing values of >50 ppm and up to 200 ppm (**figure 4h**). The Corbetti melt inclusions have the lowest Li and B concentrations (**figure 4g and h**).

5 Discussion

5.1 Characterisation of the liquid line of descent for peralkaline magmas of the MER

Melt inclusion major and trace element data (**figures 2, 3**) are consistent with pantelleritic magmas being derived via protracted fractional crystallisation of a basaltic parental melt, as has been proposed in previous studies [*Hutchison et al.*, 2018; *Iddon et al.*, 2019; *Peccerillo et al.*, 2003]. However, there is some variance in the trace element systematics e.g. changes in slope with increasing Zr, or variability at fixed Zr outside the analytical error (**figure 3**).

Fractional crystallisation models were constructed to characterise the liquid line of descent to confirm the relationship between the basaltic and pantelleritic samples (**figure 3**). The proportion of crystallising phases required to describe the liquid line of descent observed in the major element data was determined using Principal Component Analysis (PCA) [*Maclennan et al.*, 2001; *Neave et al.*, 2012] (**Supplementary Material**). The Kone sample set was used for PCA analysis as it is most complete. Results for the other sample sets are provided in the **Supplementary Material**. The results of the analysis suggest that the mafic data array can be explained by the progressive removal of up to 59% clinopyroxene ($En_{32}Wo_{53}Fs_{15}$), 40% plagioclase feldspar ($An_{85}Ab_{15}Or_{0.4}$), 0.8% olivine (Fo_{75}), 0.4% magnetite and accessory apatite. The change in melt composition over the Daly Gap may be explained by the removal of 54% plagioclase ($An_{85}Ab_{15}Or_{0.4}$), 32% clinopyroxene ($En_{32}Wo_{53}Fs_{15}$), 8% olivine (Fo_{80}), 5% magnetite, and 1% apatite. The trachytic array may be explained by the removal of 85% alkali feldspar ($An_2Ab_{74}Or_{24}$), 11% fayalite ($Fo_{1.3}$), 0.3% pyroxene ($En_5Wo_{43}Fs_{52}$), 2% ilmenite, and 1% apatite. The rhyolitic array may be explained by the removal of 78% alkali feldspar ($An_2Ab_{74}Or_{24}$), 3% pyroxene ($En_2Wo_{41}Fs_{57}$), and 19% aenigmatite. PCA root mean square fits are $1.4x10^{-8}$, $1.1x10^{-10}$, $1.8x10^{-9}$, and 0.002 respectively. Lower numbers indicate better fits, values <0.01 are deemed reasonable.

These results are consistent with fractional crystallisation models produced for pantellerite magmas in other studies. For example, Peccerillo et al. [*2003*] modelled a fractionation assemblage made up of 85-90% alkali feldspar, 10% clinopyroxene, 2% fayalite, and 2% Fe-Ti oxides, in the later stages of melt evolution at Gedemsa (**figure 1**). Meanwhile the dominance of plagioclase over the Daly Gap, and the change from fayalite to aenigmatite crystallisation in the rhyolitic array is similar to model results from Pantelleria [*Neave et al.*, 2012; *White et al.*, 2009]. The results for the basaltic array are less consistent with published examples, with models for Gedemsa and southern and northern portions of the WFB calling

for a greater degree of olivine and plagioclase fractionation [*Peccerillo et al.*, 2003; *Rooney et al.*, 2007; *Trua et al.*, 1999]. Peccerillo et al. [*2003*] suggests that greater plagioclase and olivine fractionation reflects shallower storage conditions.

5.2 Modelling Trace Element Behaviour

To model trace element behaviour during fractional crystallisation of MER magmas, the Rayleigh fractional crystallisation equation was used:

$$\frac{C_i^l}{C_i^0} = F^{D-1}$$

, where i is the element of interest; C_i^0 is the original concentration of element i in the parental liquid; C_i^l is the concentration in the liquid; D is the solid-melt partition coefficient; and F is the fraction of liquid remaining. Bulk partition coefficients were calculated based on the phase assemblages predicted down the liquid line of descent and observed mineral-melt partitioning data collated from [*Bacon and Druitt*, 1988; *Bindeman and Davis*, 2000; *Blundy and Wood*, 1991; *Bougault and Hekinian*, 1974; *Dawson and Hinton*, 2003; *Ewart and Griffin*, 1994; *Fujimaki*, 1986; *Gaetani and Grove*, 1995; *Green et al.*, 1993; *Henderson and Pierozynski*, 2012; *Hill et al.*, 2000; *Klemme and Dalpé*, 2003; *Larsen*, 1979; *Lemarchand et al.*, 1987; *Luhr et al.*, 1984; *Mahood and Stimac*, 1990; *Mathez and Webster*, 2005; *McCubbin et al.*, 2015; *Nagasawa*, 1970; *Nagasawa and Schnetzler*, 1971; *Neave et al.*, 2012; *Nikogosian and Sobolev*, 1997; *Parat and Holtz*, 2004; *Paster et al.*, 1974; *Peccerillo et al.*, 2003; *Stix and Gorton*, 1990; *Villemant*, 1988; *Villemant et al.*, 1981; *Webster et al.*, 2009; *Webster et al.*, 2017; *White et al.*, 2009; *Wood and Trigila*, 2001]. See **Supplementary Material** for the full list of partition coefficients used. Feldspar-melt partition coefficients for Sr, Ba, and Rb were additionally calculated using empirically determined equations for plagioclase from [*Blundy and Wood*, 1991] and [*Henderson and Pierozynski*, 2012]. As Zr is highly incompatible in peralkaline rocks, it was used as a fractionation index. The trachytic samples can be generated by ~85% fractional crystallisation of the mafic parental melts. The pantelleritic rhyolites require a further 40% crystallisation. The total amount of fractional crystallisation required is therefore ~91%. Peccerillo et al. [*2003*] and [*Gleeson et al.*, 2017] estimated that pantellerites from Gedemsa and Aluto could be generated from a basaltic

parent after ~90% fractionation. The pantellerites continue to fractionate, with a total fractionation of 93-94% predicted for some samples (**figure 4**).

Incompatible trace element variations are well explained by protracted fractional crystallisation of a basaltic parent (**figure 3**). The slight deviation from linear patterns can be explained by the crystallisation of apatite, which has high partition coefficients for REE of ~7-40 [*Mahood and Stimac*, 1990]. Variations in apatite crystallisation cannot account for the enrichment in just the medium and heavy REEs seen in the Aluto, BVF, and Fentale samples (**figure 3**). Reduced clinopyroxene fractionation may also occur during this interval. Clinopyroxene-melt partition coefficients for the medium and heavy REEs become larger as the pyroxene Na content increases. The pyroxenes evolve eventually to aegirine augites in peralkaline systems [*Fedele et al.*, 2009; *Marks et al.*, 2004]. This is due to an increased preference for these elements in the mineral structure [*Marks et al.*, 2004].

The compatible trace elements are consistent with fractional crystallisation. Plagioclase-melt partition coefficients for the LILEs are controlled by feldspar An content and temperature [*Blundy and Wood*, 1991]. Alkali feldspar-melt partition coefficients for Ba and Sr are controlled by melt peralkalinity and temperature; for Rb they are controlled by mineral Or content [*Henderson and Pierozynski*, 2012]. The spread in Rb, Ba (**figure 3**) and Eu (**Supplementary Material**) may be explained by variable amounts of feldspar crystallisation, as well as changing partitioning behaviour during the evolution between basaltic and trachytic melts. The greater spread in Ba in the most evolved samples is consistent with variability in the partition coefficients in line with observed variations in melt peralkalinity (**figure 3b**) [*Henderson and Pierozynski*, 2012]. The observed variation in feldspar Or content cannot, however, account for the spread in Kone Rb data (**figure 3a**), suggesting additional sources of enrichment/depletion.

The effect of feldspar resorption was modelled for Ba and Rb, both strongly compatible in feldspar (**figure 3a, b**). Feldspar Ba compositions from the Afar were used for the modeling [*Barberi et al.*, 1975]. Whilst the large spread in Ba for both Kone and Fentale quartz-hosted melt inclusions is consistent with small amounts of feldspar resorption (~10-20%), the model for Rb does not produce such a good fit for the Kone melts (**figure 3a, b**). Alkali feldspar

resorption occurred in the central Kenya peralkaline province, based on anomalous Ba enrichments [*Macdonald and Bagiński*, 2009]. Peccerillo et al. [*2003*] have linked high Ba concentration in trachytes from Gedemsa to feldspar accumulation.

5.3 Reconstructing primary melt volatile contents and degassing behaviour

5.3.1 H_2O and CO_2 systematics and estimates of magma storage depths

Volatile elements will behave like incompatible elements during fractional crystallisation, if the melts are volatile-undersaturated. Mineral-melt volatile partitioning is assumed to be negligible in most phases. Partitioning of water into apatite, as a nominally hydrous mineral with an affinity for halogens, was considered [*Mathez and Webster*, 2005; *Webster et al.*, 2009]. Fractional crystallisation models for H_2O and CO_2 are marked on **figure 4a-c**; the data lie far below the modelled liquid line of descent, suggesting that the melts were saturated with an exsolved volatile phase during fractionation, even for the most primitive melts. The range in CO_2 contents is largely due to degassing CO_2 into an exsolved volatile phase; there may also, however, be some sequestration of CO_2 into a shrinkage bubble [*Hartley et al.*, 2014], perhaps driven by post-entrapment crystallisation [*Steele-Macinnis et al.*, 2011].

The pressure dependence of H_2O-CO_2 solubility [*Papale*, 1999] suggest that the on-axis evolved silicic melts, from (**figure 5b**) are stored at lower pressures in the crust than the mafic parental melts (**figure 5a**). The olivine-hosted melt inclusions from the on-axis volcanic centre (Kone) record volatile contents consistent with storage pressures of up to ~350 MPa (**figure 5a**), equivalent to a depth of ~13 km in the crust assuming an average crustal density of 2800 kgm^{-3} [*Wilks et al.*, 2017] and a temperature of 1170 °C, estimated based on clinopyroxene-liquid thermometry [*Iddon et al.*, 2019]. The quartz-hosted melt inclusions from the on-axis centres record volatile contents consistent with storage pressures of up to ~300 MPa (**figure 5b**), equivalent to a depth of up to ~11 km in the crust, assuming a temperature of ~765 °C [*Gleeson et al.*, 2017] (upper bounds). There is significant overlap between both datasets, but this may be due to post-entrapment modification of CO_2 contents in the olivine-hosted melt inclusions, H^+ loss from the inclusions [*Bucholz et al.*, 2013], or to magmas being stored at a range of depths. Corbetti and Fentale quartz-hosted melt inclusions record slightly lower values for H_2O at similar CO_2 contents to the Kone and Aluto samples,

which might suggest shallower storage pressures of ~170 MPa (**figure 5b**), equivalent to a depth of 6 km in the crust.

The olivine-hosted melt inclusions from the off-axis BVF volcanic field record volatile contents consistent with slightly deeper storage pressures of up to ~500 MPa (**figure 5a**), equivalent to a depth of 18 km in the crust, assuming a temperature of 1170 °C [*Iddon et al.*, 2019]. These depth estimates are consistent with the suggestion of deeper fractionation of off-axis melts [*Rooney et al.*, 2007]. Using a structural clinopyroxene-only geobarometer [*Nimis and Ulmer*, 1998] Rooney et al. [*2007*] estimated storage depths of <10 km for the axis-central Wonji Fault Belt (WFB) basalts, but storage depths of up to 35 km for the off-axis melts. Our estimates of storage depths based on H_2O-CO_2 barometry are minima. Clinopyroxene-liquid geobarometry [*Neave and Putirka*, 2017] indicates deeper storage of Kone mafic melts, at up to 21 km [*Iddon et al.*, 2019]. Basalts appear to be sourced from complex, multi-levelled storage systems both on and off the rift axis.

The melt inclusions show evidence of extensive degassing. We may use the ratios of volatile to non-volatile elements that are thought to behave similarly (i.e. during crystallisation and melting) to estimate original H_2O and CO_2 concentrations in primitive basalt melts [*Rosenthal et al.*, 2015]. Ratios of CO_2 to incompatible elements such as Nb [*Saal et al.*, 2002] or Ba [*Hauri et al.*, 2019; *Le Voyer et al.*, 2017] are typically used to make estimates of primary melt CO_2. Ratios of H_2O to LREEs (La, Ce, Nd) are used to make estimates of primary melt H_2O [*Dixon et al.*, 2002; *Michael*, 1995]. Rosenthal et al. [*2015*] suggest a range of CO_2/Ba ratios for non-enriched and enriched depleted mantle (DMM) from ~130 to ~150 (**figure 6a**). Saal et al. [*2002*] and Le Voyer et al. [*2019*] suggest values closer to 100 (**figure 6a**). Assuming CO_2/Ba ratios of 100 and 140 (**figure 6a**) the on-axis WFB basalt primary melt is estimated to have contained 1.8 and 2.5 wt.% CO_2 respectively. The off-axis primary melt is estimated to have contained between 0.7 and 1 wt.% CO_2. These estimates suggest that between ~1.5 and ~2.2 wt.% CO_2 has been lost from the WFB basalts prior to eruption, and presumably prior to fractionation; and between ~0.2 and ~0.5 wt.% CO_2 is estimated to have been lost from the off-axis melts prior to eruption.

Estimates of H_2O/Ce for depleted mantle range from 150 ± 10 [*Dixon et al.*, 2002] to 245 ± 12 [*Le Voyer et al.*, 2017] (**figure 6b**). If we assume similar primary melt ratios for the MER melts, the WFB basalt primary melt is estimated to have contained 0.8-1.2 wt.% H_2O. The off-axis primary melt is estimated to have contained between 0.6 wt.% and 0.8 wt.% H_2O. This suggests that minimal H_2O has been lost from the basalts prior to eruption (which is consistent with the high pressure of storage and high solubility of H_2O), or that the H_2O/Ce ratios presented in the literature are inappropriate for continental rift settings. In all likelihood this applies to the CO_2/Ba ratios as well. Global variation in H_2O/Ce ratios are apparent, with a much higher H_2O/Ce ratio of 400 reported for HIMU-influenced MORB from the equatorial Atlantic [*Kendrick et al.*, 2017] and for basalts sourced from 'plume' mantle sources (Hauri et al., 2019). Ethiopian basalts are thought to be derived from melting induced by the impact of a plume at the base of the subcontinental lithospheric mantle [*Rooney et al.*, 2011].

5.3.2 Sulfur degassing and sulfide saturation

Fractional crystallisation models reproduce the sulfur concentrations in the olivine-hosted melt inclusions, but significantly overpredict the sulfur contents of the quartz-hosted melt inclusions (**figure 4d**). The behavior of sulfur is complex; at sulfide saturation it partitions between an exsolved volatile phase as well as an immiscible sulfide liquid or mineral phase, depending on temperature, or a sulfate-bearing phase depending on redox conditions. Under reducing conditions sulfide (S^{2-}) is the dominant sulfur species [*Carroll and Rutherford*, 1987; *Mavrogenes and O'Neill*, 1999]. At higher oxidation states S^{6+} becomes the dominant species [*Fortin et al.*, 2015; *Jugo*, 2009; *Li et al.*, 2009]. Our data suggests that sulfur behaves incompatibly in the mafic melts (i.e. the melt does not reach saturation in either a solid or liquid immiscible sulfide/sulfate phase nor an exsolved sulfur-bearing volatile phase) before concentrations drop dramatically in the quartz-hosted melt inclusions, down to < 0.2 wt.% (**figure 4d**).

The sulfur concentration at sulfide saturation (SCSS) was estimated using a number of models [*Fortin et al.*, 2015; *Li et al.*, 2009] (**figure 4d**). The oxygen fugacities of MER magmas are thought to be within one log unit of the QFM buffer (QFM to QFM+1; [*Gleeson et al.*, 2017; *Iddon et al.*, 2019; *Peccerillo et al.*, 2003; *Rooney et al.*, 2007; *Rooney et al.*,

2012]. Temperatures of 1170 °C [*Iddon et al.*, 2019] and 765 °C [*Gleeson et al.*, 2017] (upper bounds), and pressures of 300 MPa and 220 MPa were assumed for the mafic and silicic compositions respectively (**figure 4d**). The modified Li and Ripley [*2009*] model [*Gleeson et al.*, 2017] shows the SCSS is higher than the sulfur concentration in the olivine-hosted melt inclusions, before dropping to closely follow the concentrations in the quartz-hosted melt inclusions. These trends indicate that melts reach sulfide saturation somewhere in the Daly Gap.

However, for the oxygen fugacity prevalent in MER magmas (~QFM) [*Gleeson et al.*, 2017; *Iddon et al.*, 2019; *Peccerillo et al.*, 2003; *Rooney et al.*, 2007; *Rooney et al.*, 2012], the model by Jugo et al [*2010*] is preferred. It links the SCSS with sulfur content at anhydrite saturation (SCAS), predicting an exponential increase in the SCSS with increasing fO_2 from QFM because of the contribution of sulfate [*Jugo et al.*, 2010]. Model results for an fO_2 of QFM are similar, this time plotting much higher than the sulfur concentration in the olivine-hosted melt inclusions, but again following the sulfur concentration in the quartz-hosted melt inclusions (**figure 4d**). The depletion of chalcophile elements such as copper observed in the peralkaline rhyolites (see **Supplementary Material**) provides further evidence for the formation of a liquid immiscible or mineral sulfur-bearing phase at some point during magma fractionation over the Daly Gap. Scaillet and MacDonald [*2006*] investigated experimentally the partitioning of sulfur between melt and sulfide or sulfate for peralkaline rhyolites. They determined that, for all values of fO_2, peralkaline melts can carry between 5 and 20 times more sulfur than their metaluminous equivalents before reaching sulfide saturation.

Once there is a free exsolved volatile phase, sulfur will further partition into it. Scaillet and MacDonald (2006) have investigated experimentally the partitioning of sulfur between melt and the exsolved fluid phase. For a pantellerite at temperatures of 765 °C and an fO_2 of QFM, a fluid-melt partition coefficient, D^{f-m}, of ~50 might be expected [*Scaillet and Macdonald*, 2006]. Experiments suggest that after 80% crystallisation of a basaltic alkaline melt containing 1000 ppm S and 1 wt% H_2O, between 60 and 90% of the bulk sulfur partitions into the aqueous fluid. We calculate the mass of sulfur that partitions into the fluid phase using the difference between the fractional crystallisation model and the observed melt S concentrations. The bulk sulfur contents in the melt-sulfide-exsolved volatile phase after 94%

crystallisation would be ~ 6 wt%. This sulfur is partitioned between the melt sulfur, solid and liquid immiscible sulfur-bearing phases, and the exsolved volatile phase. For an average melt S content of 340 ppm in the peralkaline rhyolitic melts, an exsolved volatile phase might contain 1.7 wt.%, with the remaining 4.3% sequestered in the solid and/or liquid immiscible sulfur-bearing phases.

5.3.3 Behaviour of halogens and lithium during differentiation and degassing

Fractional crystallisation models reproduce well the incompatibility of Cl in the mafic melts; however, they fail to predict the lower chlorine concentrations observed in the evolved peralkaline melts (**figure 4e**), which suggests that chlorine is being lost to another phase. Cl partitioning into apatite is included in the model (see **Supplementary Material** for partition coefficients), but there may be loss to some other chlorine-bearing accessory mineral, such as mica [*Iddon et al., 2019*], which may not be captured. Here we consider the loss of chlorine to an exsolved volatile phase as the dominant process causing melt depletion in chlorine.

The solubility of Cl in silicate melts has a complex pressure dependence. At pressures >200 MPa it shows a negative dependence, becoming increasingly soluble in silicate melts with dropping pressure; however, this changes to a positive dependence at pressures < 200 MPa [*Lukanin*, 2015; 2016]. In a closed system, where the exsolved volatile phase is not lost, this relationship can reverse again at even shallower pressures [*Lukanin*, 2015; 2016]; this may account for the continued, if slightly subdued, rise in melt Cl contents following the Daly Gap (**figure 4e**). However, H_2O-CO_2 solubility relationships indicate that many of the quartz-hosted melt inclusions were trapped at pressures >150 MPa (**figure 5b**). Cl solubility shows a strong compositional dependence, becoming increasingly soluble with increasing melt alkali content and decreasing silica activity [*Carroll*, 2005]. The influence of the negative temperature dependence on Cl solubility is also amplified in alkali-rich melt compositions [*Carroll and Webster*, 1994]. The quartz-hosted melt inclusions show a positive correlation between melt Cl concentration and peralkalinity (**figure 7a**).

Published experimental data for silicate melts coexisting with low-Cl fluids, or with supercritical Cl-bearing fluids show that Cl partitions strongly into aqueous fluids relative to

silicate melts by a factor of ~20 to 300 [*Kilinc and Burnham*, 1972]. For low bulk Cl contents, Cl concentrations decrease in rhyolitic melts coexisting with a single aqueous fluid phase as pressure increases from 200 to 800 MPa and the fluid/melt partition coefficient for Cl increases with increasing pressure. However, with increasing concentration of Cl in the solution at pressures below ~200 MPa, the binary system H_2O-NaCl is characterized by an immiscibility gap (a subcritical region) where a Cl-poor aqueous fluid coexists with a Cl-rich hydrosaline brine [*Carroll*, 2005]. The compositions of the aqueous fluid and the brine are invariant at constant pressure and temperature, which means that Cl and H_2O concentrations in the fluids and the coexisting silicate melt will be fixed (Gibbs' phase rule) [*Balcone-Boissard et al.*, 2016; *Signorelli et al.*, 2001]. A constant Cl concentration in the melt as more Cl is added to the system is the typical expression of the melt being saturated with both a hydrosaline liquid and an H_2O-rich aqueous fluid and this behaviour defines the solubility limit for Cl [*Carroll*, 2005; *Shinohara*, 1994; *Signorelli and Carroll*, 2002].

The MER data show an increase in Cl with melt evolution, with no plateau, suggesting that perhaps formation of a chlorine-bearing hydrosaline brine does not occur at the pressures of melt inclusion entrapment (**figure 4e**). The Cl solubility model by Webster et al. [*2015*] was established using experiments in which the solubility of Cl was determined for silicate melts saturated in a hydrosaline brine, with or without a coexisting vapour phase. The modelled Cl solubilities, assuming temperatures of 1170 °C [*Iddon et al., 2019*] and 765 °C [*Gleeson et al., 2017*, upper bounds], and pressures of 300 MPa and 220 MPa for the mafic and silicic compositions respectively, are much higher than the observed data for the MER melt inclusions (**figure 4e**). This suggests that hydrosaline brine formation does not occur. Instead the trends in the data are consistent with the partitioning of chlorine into an exsolved supercritical fluid phase.

The fractional crystallisation models accurately reproduce the incompatibility of F in the mafic melts but fail to predict the lower F contents in the evolved peralkaline melts (**figure 4f**). As F partitioning into apatite is considered by the crystallisation model, and there is no evidence for fluorine-bearing phases such as fluorite, loss to an exsolved volatile phase is considered. F solubility is generally high in silicate melts but could be reduced by the rapid increase in SiO_2 driven by fractional crystallisation over the Daly Gap (**figure 2**). Increasing

melt polymerisation has been linked to increased F partitioning into an exsolved volatile phase [*Bailey*, 1977; *Martini*, 1984]. The low halogen contents of melt inclusions at Corbetti relative to the other datasets may be a consequence of lower melt peralkalinity (**figure 4e and f**). This cannot account for the situation at Fentale where Cl contents, along with melt peralkalinity, are in line with Kone and Aluto samples (**figure 4e**).

The total mass of chlorine and fluorine partitioned into the aqueous fluid phase may be estimated using the difference between the fractional crystallisation models and the observed concentrations. This analysis yields apparent fluid-melt partition coefficients ($D^{f\text{-}m}$) of 1.75 for F, and 3 for Cl, consistent with experimentally determined results [*Borodulin et al.*, 2009; *Iveson et al.*, 2017]. Borodulin et al. [*2009*] carried out experiments on F partitioning between high-silica peralkaline rhyolites and aqueous fluids at 750°C and 100 MPa suggesting a $D^{f\text{-}m}$ of 1.7±1.6. Iveson et al. [*2017*] conducted experiments at 810-860°C, 150-405 MPa and fO_2 NNO-0.5 to NNO+2 on hydrous rhyodacites showing that Cl strongly partitions into a fluid over a melt phase with a $D^{f\text{-}m}$ ranging from 3.5 to 22.7. This partitioning of Cl into an exsolved volatile phase is thought to remain > 700 MPa; at lower pressures partitioning towards melt has been observed to increase [*Kilinc and Burnham*, 1972]. **Figures 7c** and **7d** shows the relationship between the halogens and melt H_2O contents. Constant melt Cl and F above 2 wt.% H_2O demonstrates that melt concentrations are being buffered by a single supercritical fluid phase.

Whilst the fractional crystallisation model provides a reasonable fit to the observed Li data, suggesting it behaves relatively incompatibly, the spread in the data might be explained by semi-volatile behaviour (**figure 4h**). Some of the quartz-hosted melt inclusions show Li enrichment over that predicted from fractional crystallisation, examples from Fentale show a corresponding slight enrichment in CO_2 and depletion in H_2O in comparison to the other datapoints. Li is complex, as at shallow crustal pressures it can partition into a number of mineral phases [*Bindeman and Davis*, 2000; *Nikogosian and Sobolev*, 1997], but has also been observed to behave as a volatile element in some H_2O-rich magmas. It has been suggested that Li may diffuse into an exsolved volatile phase as rapidly as water [*Koga et al.*, 2008], whilst other experimental studies have shown that in silica-rich magmas Li will preferentially partition into a volatile-bearing fluid over the melt [*Kent et al.*, 2007],

particularly in the presence of chlorine [*Webster et al.*, 1989]. At Mount St Helens melt inclusion enrichment in Li has been attributed to shallow accumulation of CO_2-rich fluids from deeper degassing magmas and rapid diffusive re-equilibration of the melt inclusions [*Berlo et al.*, 2004]. At Pantelleria, Neave et al [*2012*] explain Li enrichment in melt inclusions by entrapment in the presence of a Cl-rich brine.

5.4 Predicted volatile outgassing during explosive MER peralkaline eruptions

If we assume that the system is closed with no passive degassing, the fractional crystallisation models for Kone may be used to calculate the volume of pre-eruptive volatiles exsolved during the evolution from a basaltic parent to a pantelleritic rhyolite melt. The proportions of the different volatile species in the exsolved volatile phase can also be estimated. The H_2O contents of the basaltic parental melts is ~1.2 wt.% which, under conditions of no degassing and complete incompatibility, would increase to 55 wt.% in the residual melt after ~94% crystallisation (**figure 4b**). The melts actually hold ~7 wt.% H_2O after 94% crystallisation at 220 MPa (**figure 5b**), which means that the remainder has exsolved for these pressure conditions. In reality, migration of an exsolved volatile phase would likely occur over long timescales during fractionation. For this reason we predict the mass of the H_2O and CO_2 in the pre-eruptive exsolved volatile phase in the peralkaline rhyolite based on the quartz-hosted melt inclusions alone, assuming that any exsolved volatiles that existed prior to the Daly Gap will have been lost to outgassing during decompression of the low viscosity melt on ascent to shallower storage regions and over the long course of evolution (**figure 4a and c**). The pervasive loss of deep-derived exsolved volatiles from stored magmas is consistent with the diffuse degassing of a CO_2-rich magmatic gas observed over much of the MER [*Hunt et al.*, 2017; *Hutchison et al.*, 2016a]. We calculate that, after fractionation from trachytic to evolved pantelleritic melt (~60% crystallisation) and with no degassing, H_2O contents would rise from 7 wt.% to 17 wt.% and CO_2 contents would rise from 0.02 wt.% to 0.05 wt.%. As the melts hold ~7 wt.% H_2O and ~0.025 wt.% CO_2 after 94% crystallisation at 220 MPa (**figure 5b**), this means that ~10 wt.% H_2O and ~0.025 wt.% CO_2 will have been exsolved from the rhyolite for these pressure conditions.

Using the same method for the halogens, but assuming volatile retention in the mafic melts (**figure 4e and f**), we find that this exsolved volatile phase will also contain 0.7 wt.% F, and

629 0.6 wt.% Cl. Exsolved S contents of 1.7 wt.% were estimated based on measured values of
630 ~340 ppm in melt inclusions and experimental fluid-melt partition coefficients [*Scaillet and*
631 *Macdonald*, 2006]. We therefore estimate that a total exsolved volatile phase of ~13 wt.%
632 may develop during late-stage fractionation crystallisation, which is equivalent to ~4.5 vol.%
633 (from the Ideal Gas Law) at a pressure of 220 MPa and temperature of 765 °C [*Gleeson et*
634 *al., 2017*, upper bounds].

635

636 The mass of the exsolved volatile phase may be used to make estimates of the potential yield
637 of an explosive peralkaline eruption at one of the MER calderas. Caldera-forming eruptions
638 may have produced >10 km^3 eruptive volume [*Hutchison et al.*, 2016b]. Assuming an
639 average bulk magma density of 2300 kg/m^3, we calculate a volatile yield of 2300 Mt H_2O
640 (where 1 Mt is equal to 1 x 10^{12} kg), 6 Mt CO_2, 390 Mt S, 150 Mt F, and 150 Mt Cl for an
641 eruption of 10 km^3 peralkaline magma. An additional component from syn-eruptive
642 degassing by exsolution can also be estimated, recorded in the difference between the matrix
643 glass and melt inclusion compositions. Whilst F and Cl contents appear similar, matrix
644 glasses show on average a ~50 ppm difference in S. Assuming that melt H_2O and CO_2
645 retention at atmospheric pressure is minimal, a melt fraction of 65 vol.% for the erupted
646 magma, and a melt density of 2275 kg/m^3, a syn-eruptive degassing (from exsolution) of 365
647 MT of H_2O, 1 Mt of CO_2, and 0.5 Mt of S is estimated. This brings the estimated total
648 volatile yield for an explosive peralkaline eruption to 2665 Mt H_2O, 7 Mt CO_2, 390.5 Mt S,
649 150 Mt F, and 150 Mt Cl, for eruptions of 10 km^3. Post-caldera eruptions are much smaller
650 (between 0.01-1 km^3) [*Hutchison et al.*, 2016b], and are typically crystal-poor. Making
651 similar assumptions, but with a melt fraction of 90 vol.% for the erupted magma, the
652 estimated total volatile yield for a post-caldera peralkaline eruption would be 3-265 Mt H_2O,
653 <0.01-0.7 Mt CO_2, 0.4-40 Mt S, 0.2-15 Mt F, and 0.2-15 Mt Cl.

654

655 The much larger Tambora eruption of 1815 (~50 km^3) [*Oppenheimer*, 2003] is thought to
656 have released ~100 Mt Cl, 70 Mt F, and 60 Mt S [*Sigurdsson and Carey*, 1992] and the S
657 release from Mount Pinatubo (~20 km^3) has been estimated at 10 Mt [*Gerlach et al.*, 1996;
658 *Wallace and Gerlach*, 1994]. This suggests that the output of S and halogens may be more
659 significant from peralkaline explosive eruptions, such as those during the formation of the
660 MER calderas, than from their metaluminous and peraluminous counterparts. Neave et al.

[*2012*] highlighted this in their estimates of the S yield from Pantelleria, predicting the release of 80-160 Mt S during the eruption of the 7 km^3 Green Tuff. They interpreted the higher yields of sulfur as relating to high sulfur concentrations at sulfide saturation combined with high fluid/melt partition coefficients, allowing peralkaline melts to retain sulfur for longer during their early differentiation and then release it into aqueous exsolved fluids [*Scaillet and Macdonald, 2006*]. Alkali-related halogen retention and high initial parental melt volatile contents, perhaps due to small fraction melting of enriched subcontinental lithospheric mantle, may also play a role in increasing predicted volatile outputs. Our results further suggest that large, explosive continental rift-related eruptions may be significant sources of HCl into the upper troposphere or stratosphere. Injection of HCl into the stratosphere has also been linked to the ozone destruction and, in the troposphere, to the production of acid rain [*Kutterolf et al.*, 2013].

5.5 Implications of our results for MER Magma Storage

We interpret the behaviour of the volatile species, in particular the timing of volatile saturation and the various controls on melt volatile solubilities, as providing evidence for a vertically extended magmatic storage system beneath the MER (**figure 8**). Mafic magma batches, both on- and off-axis, are stored at depths extending down to 18 km in the crust, and potentially deeper, where they are saturated with an exsolved volatile phase (**figure 5a**). Over the course of the Daly Gap, from which melts are not preserved, on-axis magmas saturate in both an exsolved volatile phase and in sulfide. Settling of sulfides and growth of finely disseminated bubbles in the magma will lower bulk magma density, promoting its rise to shallower depths of ~8-6 km. Cl and F partition into the exsolved volatile phase with fluid-melt partition coefficients of ~3 and ~1.75 (**figure 8**) (Kilinc and Burnham, 1972; Shinohara et al., 1989). In the shallower parts of the reservoir fractional crystallisation drives the magma composition towards rhyolite, generating extensive crystal mushes. The substantial exsolved volatile phase may accumulate to form a low density, gas-rich roof zone. Continued fractional crystallisation leads to melts becoming peralkaline, thus increasing halogen solubility in the melt (**figure 7a, b**) (Anfiligov et al., 1973; Carroll, 2005; Glyuk, 1980). There may also be evidence in some cases for the accumulation of exsolved volatiles from deeper degassing magmas (**figure 4h**). This might suggest magmatic recharge or mafic underplating occurs.

Magmatic evolution at multiple storage depths has been proposed for other peralkaline systems in the MER and wider EARS based on petrological evidence. Rooney et al. (2012) suggested a two-step polybaric process at Chefe Donsa, with fractionation of basalts at mid-upper crustal depths occurring prior to extraction and ascent of those liquids to form a second trachytic-rhyolitic fractionating storage region. Rooney et al. (2012) highlight the importance of exsolved volatiles in controlling the eruptibility of intermediate magmas. MacDonald et al. (2008) postulate that a region of several dynamic, interacting, independent reservoirs and conduits, stretching down to depths of 10 km in the crust, feeds the Greater Olkaria volcanic complex. Again, they highlight the influence of an exsolved volatile-rich phase, with negative Ce anomalies linked to an oxidising, halogen-rich exsolved volatile phase (Macdonald et al., 2008). Direct evidence of volatile loss is also observed, with vesiculation common at the borders between magmatic inclusions and comenditic hosts (Macdonald et al., 2008). Macdonald et al. (2012) suggest that mafic recharge and underplating may be a fundamental source of volatiles for the Greater Olkaria volcanic complex.

5.6 Magma fluxes in the MER

The mass of a pre-eruptive exsolved volatile phase was calculated based on the assumption that any exsolved volatile phase that existed prior to the Daly Gap will have been lost through outgassing. Lee et al. (2016) examined the diffuse soil degassing in the Magadi-Natron Basin, on the border between Kenya and Tanzania, linking the loss of 4 Mt/yr CO_2 to the extensional tectonics of the EARS. Extrapolation of their results provides estimates for a CO_2 flux on the order of tens of Mt per year for the entire Eastern branch of the EARS, comparable to emissions from the global mid-ocean ridge system (53-97 Mt/yr; Lee et al., 2016). Numerous authors have highlighted the importance of structural controls on fluid and vapour migration in volcanic areas (Hutchison et al., 2015; Robertson et al., 2016), degassing in the MER is concentrated in discrete areas of volcanic and off-edifice activity (Hunt et al., 2017). Characterisation of these areas led Hunt et al. (2017) to estimate a much lower CO_2 flux of 0.52-4.36 MT/yr for the central and northern portions of the MER and 3.9-32.7 MT/yr for the EARS.

Taking an average CO_2 loss of 1.1 wt.% (see section 5.3.1), and assuming loss is solely via diffuse soil degassing, the CO_2 fluxes presented by Hunt et al. (2017) may be used to estimate the mass of degassing basaltic melt per year of ~45-395 Mt beneath the MER and ~355-2970 Mt beneath the EARS. Assuming a melt density of 2750 kg/m^3 and crystal densities of 3320 kg/m^3 (clinopyroxene), 3400 kg/m^3 (olivine), and 2680 kg/m^3 (plagioclase), typical phase proportions (40% plagioclase, 35% olivine and 25% clinopyroxene; Iddon et al., 2019), and a bulk crystallinity of 45%, these estimates of degassing mass of basalt equate to volumes of ~0.02-0.14 km^3 per year and ~0.1-1 km^3 per year for the MER and EARS respectively.

If we assume an average crustal thickness of 32 km for the ~1000 km long MER (Casey et al., 2006), spreading rates of ~5 mm a year (Saria et al., 2014) would require the intrusion of ~0.16 km^3 magma a year if extension was predominantly magma-assisted (Bastow et al., 2010; Keir et al., 2011; Kendall et al., 2005), comparable with the results of this study based on the upper bounds of CO_2 flux estimates (Hunt et al., 2017). Wadge et al. (2016) have documented 21 historical eruptions along the EARS over the past 200 years. A minimum of 5 km^3 of predominantly basalt was erupted on to the surface, with high intrusion/extrusion ratios (4-15; Wadge et al., 2016). Based on these figures a magma flux for the whole EARS of ~0.13-0.40 km^3/year may be estimated, which is within range of the magma degassing rates calculated above.

6. Implications for geophysical volcano monitoring

InSAR observations of volcano deformation are increasingly being used as a monitoring technique as satellite coverage grows. As a remote technique it is ideal for countries such as Ethiopia which have a high number of potentially active volcanic sites, many of which are largely inaccessible or too costly to monitor. Magma injection may cause an inflation of a volcanic edifice, whilst withdrawal might result in a period of deflation (Segall, 2013). Modelling of the spatial and temporal characteristics of the deformation signal can also be used to estimate the source depth and geometry, providing vital information about magma storage [*Biggs et al.*, 2011; *Hutchison et al.*, 2016a; *Lloyd et al.*, 2018]. Using InSAR Biggs et al. [*2011*] identified four volcanic edifices in the MER (Aluto, Corbetti, Bora, and Haledebi; see **figure 1** for locations) that have undergone significant deformation between

1993 and 2010. However, there are many factors that influence the deformation signal at a volcanic edifice. Magma rheology, edifice type, hydrothermal activity, tectonic setting, and stress fields all play a key role [*Biggs et al.*, 2014b]. Some volcanoes will show significant pre- and syn-eruptive deformation, whilst some will not [*Biggs et al., 2014*], and the volume of erupted material is often much greater than the subsurface volume change implied by the deformation [*Anderson and Segall*, 2011; *McCormick Kilbride et al.*, 2016; *Rivalta and Segall*, 2008; *Segall*, 2013].

Understanding volatile behaviour is important for the interpretation of geodetic measurements. Exsolution of magmatic gases can lead to an inflation signal not related to magma injection, and outgassing or resorption into a crystalline mush can equally cause subsidence [*Caricchi et al.*, 2014]. In these cases, a coupled geodetic and gravity survey can differentiate between the behaviour of melt and exsolved volatiles, as an exsolved volatile phase will lower the bulk magma density [*Gottsmann and Battaglia*, 2008]. The presence of a low density exsolved volatile phase will increase the compressibility of magma, which can result in muted ground displacements [*Biggs et al., 2014; McCormick-Kilbride et al., 2016*]. The difference between the volume erupted (V_e) and the subsurface volume change (ΔV) is controlled by the bulk compressibility of the magma [*Huppert and Woods*, 2002]:

$$\beta_m = \frac{1}{\beta_r} + \frac{1}{\rho}\frac{\delta\rho}{\delta P}$$

, where β_r is the effective bulk modulus of the surrounding wall rock; ρ is the bulk magma density; and P is pressure. The bulk compressibility of the country rock is also vital (Johnson, 1992):

$$\beta_c = \frac{3}{4\mu}$$

, where μ is the shear modulus of the host rock. Considering the simplest example of a spherical source, r, the ratio between V_e and ΔV (for the 'Mogi' source) [*Rivalta and Segall*, 2008]:

$$r = \frac{V_e}{\Delta V} = 1 + \frac{\beta_m}{\beta_c}$$

, would be 1 for an incompressible magma. However, a significant exsolved volatile phase will increase β_m by an order of magnitude, therefore, a large volume eruption can be

accommodated by expansion of the remaining magma, resulting in a minor volume change in the reservoir (r>>1) [*Johnson*, 1992; *McCormick Kilbride et al.*, 2016]. Country rock compressibility is different for deep prolate sources, where:

$$\beta_c = \frac{1}{\mu}$$

, is more appropriate [*Anderson and Segall, 2011; McCormick-Kilbride et al., 2016; Rivalta and Segall, 2008*]. Crustal μ is not well constrained, it may range from ~0.1 GPa for very compliant rocks to 30 GPa for much stiffer crust [*Gudmundsson*, 2005]. The exact value for β_r also varies, depending on the density of microfractures in the rock, but a value of 10^{10} Pa is typically used [*Tait et al.*, 1989]. Assumptions about geometry and material properties are important, for example a sill geometry, which is perhaps more appropriate for the MER calderas, would be significantly more compressible than a spherical source [*Biggs et al., 2011*].

Assuming no outgassing occurred, the β_m of MER magmas was calculated to be between 1.98 x 10^{-8} Pa^{-1} and 3.71 x 10^{-9} Pa^{-1} based on the results of the fractional crystallisation model and H_2O-CO_2 solubility pressure estimates. This gives predicted r values of 23-16 for depths of 3-8 km, assuming a spherical source and μ of 0.3 GPa. Assuming a prolate source these values change to 17-12. As *r* is proportional to β_m, it is predicted to decrease with increasing magma reservoir depth. This analysis suggests that the geodetic displacements observed at MER volcanoes [*Biggs et al., 2011; Hutchison et al., 2016a; Lloyd et al., 2018*] are likely muted. For a cumulative subsurface volume change of 0.013 km^3 at ~5 km depth, as observed by Hutchison et al. [*2016*] during rapid inflation events at Aluto, an eruptible volume of ~0.25 km^3 would be predicted (**figure 9**). For a subsurface volume change of 0.01 km^3/y at ~6.5 km depth, as observed by Lloyd et al. [*2018*] at Corbetti between 2009 and 2017, an eruptible volume of ~1.2 km^3 would be predicted (**figure 9**).

A number of volcanic monitoring techniques have been deployed across Ethiopia over the past decade. Mickus et al [*2007*] presented gravity data that imaged a Bouger anomaly beneath Aluto and Corbetti volcanoes that they interpreted to be high density bodies (~3000 kg/m^3) in the lower crust (7-17 km). This could imply that there was no low-density volatile-rich cap at Aluto or Corbetti during the data acquisition period (i.e. outgassing occurred), and

that any subsurface volume changes observed from the deformation data would be equivalent to the eruptible volume of magma. However, it may also imply that the features responsible for the Bouger anomaly are denser and/or deeper than modelled [*Mickus et al.*, 2007].

The lower density of an exsolved volatile phase will also dramatically lower seismic velocities [*Neuberg and O'Gorman*, 2002]. Crustal velocities are typically 5-10% higher beneath the rift axis, thought to be the result of mafic intrusions beneath the different volcanic centres [*Keranen et al.*, 2004]. However, low-velocity zones are also identified at upper crustal depths beneath these sites, with mid-crustal low-velocity zones also located beneath the WFB and SDFZ [*Kim et al.*, 2012]. Wilks et al. [*2017*] identified seismic b value anomalies in the shallow crust beneath Aluto, thought to correlate with regions of gas accumulation.

As electrical resistivity is sensitive to fluid content, magnetotelluric (MT) surveys can identify the presence of partial melt beneath volcanoes [*Johnson et al.*, 2016]. In section 3.5 it was highlighted that the electrical resistivity of a magmatic reservoir is dependent on the state of the magma itself [*Gaillard and Marziano*, 2005]. Dissolved volatiles can increase melt conductivity [*Laumonier et al.*, 2017]; however, exsolved volatile phases have low conductivities (10^{-2}-10 ohm m^{-1}). This has led to resistive regions beneath volcanoes sometimes being interpreted as gas-rich caps [*Aizawa et al.*, 2009]. This would still be consistent with the absence of increased electrical conductivity observed beneath Aluto [*Hübert et al.*, 2018; *Samrock et al.*, 2015]. However, if exsolved volatiles escape and mix with groundwater they can produce highly conductive regions of fluid [*Aizawa et al.*, 2009]. This might be observed beneath Aluto, where shallow regions of conductivity have been interpreted as relating to active hydrothermal systems [*Hübert et al., 2018; Samrock et al., 2015*].

7. Conclusions

Olivine- and quartz-hosted melt inclusions provide the first large-scale study of major, trace, and volatile element concentrations in MER melts. Modelling indicates that the pantelleritic quartz-hosted melt inclusion compositions can be achieved by protracted fractional crystallisation (>90%) of an enriched alkali-transitional basaltic parent similar to that of the

olivine-hosted melt inclusions. These parental melts are sourced from complex, vertically extended mafic magmatic systems, that exist both on- and off-axis.

Mafic melts are saturated in H_2O and CO_2 at depths of >13 km. Over the course of the Daly Gap, melts saturate in both a sulfide phase and an exsolved volatile phase, into which S and halogens partition. Sulfide settling and the formation of disseminated low density bubbles are expected to lower bulk magma density, promoting rise to shallow magma storage regions in the crust, where further fractionation is accompanied by the development of a substantial saline, exsolved volatile phase. There is no evidence of brine formation in the melt inclusion compositions. Possible fluxing of deep derived fluids is indicated by melt Li concentrations, perhaps suggesting magmatic underplating and/or magmatic recharge by more primitive compositions. Based on our results, an explosive, caldera-forming eruption (VEI >5) in the MER could outgas up to 2300 Mt H_2O, 6 Mt CO_2, 390 Mt S, 150 Mt F, and 150 Mt Cl into the lower troposphere or stratosphere. The S and halogen yield of such an eruption is significantly larger than would be expected from a metaluminous or peraluminous counterpart. These gas emissions would have severe environmental consequences and pose a risk to the health of humans and livestock in Ethiopia if they were injected into the lower troposphere.

The accumulation of a large fraction (up to 4.5 vol% or 13 wt% at 200 MPa) of a pre-eruptive exsolved volatile phase may also cause the under-estimation of intruded magma volumes by geodetic monitoring. Subsurface changes in volume of 0.013 km^3 and 0.07 km^3 at 5-6 km depth inferred from ground displacements at Aluto and Corbetti may well correspond to much larger eruptible melt volumes of 0.25 km^3 and 1.19 km^3 if a low density, compressible exsolved volatile phase is present. The characteristics of this exsolved volatile phase will also have an effect on gravity, seismic, and electrical resistivity data, so must be considered as fledgling volcanic monitoring schemes continue to be developed in Ethiopia.

A significant proportion of volatiles are also lost from deep mafic melts through diffuse degassing through the crust. Based on CO_2/Ba ratios we calculate that ~1.1 wt.% CO_2 may be lost from basalts in the MER system. This suggests that recently presented CO_2 fluxes would

require ~0.02-0.14 km^3 basaltic melt to be intruded every year beneath the MER, consistent with previous magma flux estimates of ~0.16 km^3/year for the MER [*Saria et al.*, 2014].

Acknowledgments

The Aluto samples used in this study were collected by Will Hutchison between 2012 and 2014. The Kone samples were collected by both Michael Rampey between 2001 and 2003 and Karen Fontijn and Keri McNamara in November 2015. The Fentale samples were collected by Fiona Iddon, Jonathan Hunt, and Abate Assen in October 2017. We acknowledge the expertise and assistance provided by colleagues from Addis Ababa University and the kind permission of national and regional authorities. This project, and Iddon's studentship, was funded by the Natural Environment Research Council grant NE/L013932/1 (RiftVolc). We thank Margaret Hartley and an anonymous reviewer for helpful reviews which improved the manuscript enormously. Data related to this publication is available both in the supplemental data file and at the https://www.repository.cam.ac.uk data repository.

892 **Figure captions**

893 **Figure 1:** Topographic map of the Main Ethiopian Rift (MER). Axis-central calderas are
894 outlined in dark blue, with Quaternary magmatic segments deposits highlighted in white
895 (adapted from Corti, 2008). The red lines represent the Wonji Fault Belt, where the majority
896 of extensional stress is accommodated; the black lines represent the older, less active border
897 faults (adapted from Corti, 2008).

898 **Figure 2:** Melt inclusion and matrix glass analyses. Plot a) shows the total alkalis versus
899 silica (TAS) diagram..The melt inclusions plotting in the basalt field are hosted by olivine;
900 the melt inclusions in the trachyte and rhyolite fields are hosted by quartz. Plot b) shows the
901 classification diagram for peralkaline rhyolites and trachytes [*Macdonald*, 1974]. Plots c)-k)
902 are major element variation diagrams. Two sigma errors, unless shown, are smaller than
903 symbols.

904 **Figure 3:** Trace element geochemistry for basaltic, trachytic and peralkaline rhyolitc melt
905 inclusions and matrix glasses of Main Ethiopian Rift volcanic rocks erupted from Kone,
906 Aluto, Fentale, Butajira Volcanic Field and Corbetti. Melt inclusions with Zr <500 ppm
907 hosted by Qz; Zr > 500 ppm hosted by quartz. Melt inclusion and matrix glass trace element
908 compositions plotted against Zr (a-h) and Rb/Nb plotted against Rb (i); lines show
909 compositions predicted by fractional crystallisation Rhyolite-Melts models [*Ghiorso and*
910 *Gualda*, 2015] for Kone. The lines distinguished by crosses show feldspar assimilation
911 models for Kone and Fentale (a and b). The shaded region in i shows the field of Precambrian
912 basement [*Peccerillo et al.*, 1998].

913 **Figure 4:** Melt inclusion and matrix glass volatile element compositions plotted against Zr;
914 the degree of fractionation, predicted from trace element behavior, is shown along the top.
915 The black lines show where fractional crystallisation has been calculated using the most
916 primitive melt after the Daly Gap and blue lines show predicted melt compositions during
917 fractional crystallisation in the presence of an exsolved volatile phase. Bulk fluid-melt
918 partition coefficients (from +1 to 0) for the models are shown above relevant lines. The
919 dotted black lines (c) show the sulfur content at sulfide saturation (SCSS), as predicted by the
920 models of Fortin et al. (2015) and Jugo et al. (2010) respectively. The red solid line (d) shows
921 Cl melt solubility as predicted by the model of Webster et al. (2015).

922 **Figure 5:** Plots of melt CO_2 content versus melt H_2O content (wt%) for a) olivine-hosted
923 melt inclusions and b) quartz-hosted melt inclusions. Melt storage pressure conditions

estimated using Papale [*1999*]. Isobars for mafic melt storage were calculated based on a temperature of 1170 °C [*Iddon et al.*, 2019], and for evolved melt storage a temperature of ~765 °C (upper bounds) [*Gleeson et al.*, 2017] was assumed. c) Depths of magma storage (assuming a crustal density of 2800 gm^{-3}) [*Wilks et al.*, 2017] plotted against longitude.

Figure 6: Ratios of volatile to non-volatile incompatible elements in Main Ethiopian Rift melt inclusions. CO_2/Ba ratios (a) are used to estimate original CO_2 concentrations in primary melts; ratios for enriched [*Rosenthal et al.*, 2015] and non-enriched primary melts [*Saal et al.*, 2002] are shown by dashed lines. H_2O/Ce ratios (b) are used to estimate original H_2O concentrations in primary melts; estimates of primary melts [*Dixon et al.*, 2002; *Le Voyer et al.*, 2017] are shown by dashed lines.

Figure 7: Halogen contents against peralkalinity in Main Ethiopian Rift melt inclusions (a-b), expressed as the agpaitic index (A.I., defined by molar (Na + K)/Al), and H_2O contents (c-d).

Figure 8: Schematic showing a vertically extended magmatic system beneath the MER. Mafic melts, saturated in H_2O and CO_2, are stored down to at least 15 km beneath both the axis-central caldera systems (right) and off-axis volcanic fields (left). Magmas become saturated in sulfide (which may settle out) and an exsolved volatile phase within the Daly Gap, which may promote magma buoyancy and rapid rise through the crust. Beneath the axis-central calderas melts rise to 6-8 km depth, where they begin to fractionate. Highly evolved residual liquids (peralkaline rhyolites) develop in an extensive mush-rich reservoir and a volatile-rich roof zone may form. Mafic melts are forced to erupt around the shadow zone, external of caldera margins. Mafic recharge may also result in the fluxing of deep CO_2- and Li-rich fluids to shallower levels. The exsolved volatiles are thought to interact with active hydrothermal systems, whilst intense pre- and syn-rift faulting also likely aids outgassing (white arrows).

Figure 9: Plot showing the changes in volume observed using InSAR at Aluto and Corbetti volcanoes over the past decade. Based on the assumption that no outgassing has occurred, r values (real magma volume change/observed volume change from InSAR) were predicted at a depth of ~5 km for Aluto and ~6.5 km for Corbetti. The eruption volumes these correspond to predict that large volumes of eruptible magma may be responsible for much smaller changes in volume observed at the surface due to the enhanced compressibility of vapour-bearing magma.

References

Abebe, B., V. Acocella, T. Korme, and D. Ayalew (2007), Quaternary faulting and volcanism in the Main Ethiopian Rift, Journal of African Earth Sciences, 48(2-3), 115-124.

Agostini, A., M. Bonini, G. Corti, F. Sani, and F. Mazzarini (2011), Fault architecture in the Main Ethiopian Rift and comparison with experimental models: implications for rift evolution and Nubia–Somalia kinematics, Earth and Planetary Science Letters, 301(3-4), 479-492.

Aizawa, K., Y. Ogawa, and T. Ishido (2009), Groundwater flow and hydrothermal systems within volcanic edifices: Delineation by electric self-potential and magnetotellurics, Journal of Geophysical Research: Solid Earth, 114(B1).

Anderson, K., and P. Segall (2011), Physics-based models of ground deformation and extrusion rate at effusively erupting volcanoes, Journal of Geophysical Research: Solid Earth, 116(B7).

Bachmann, O., M. A. Dungan, and P. W. Lipman (2002), The Fish Canyon magma body, San Juan volcanic field, Colorado: rejuvenation and eruption of an upper-crustal batholith, Journal of Petrology, 43(8), 1469-1503.

Bacon, C. R., and T. H. Druitt (1988), Compositional evolution of the zoned calcalkaline magma chamber of Mount Mazama, Crater Lake, Oregon, Contr. Mineral. and Petrol., 98(2), 224-256.

Bailey, J. C. (1977), Fluorine in granitic rocks and melts: a review, Chemical Geology, 19(1-4), 1-42.

Balcone-Boissard, H., G. Boudon, R. Cioni, J. Webster, G. Zdanowicz, G. Orsi, and L. Civetta (2016), Chlorine as a geobarometer for alkaline magmas: Evidence from a systematic study of the eruptions of Mount Somma-Vesuvius, Scientific reports, 6, 21726.

Barberi, F., G. Ferrara, R. Santacroce, M. Treuil, and J. Varet (1975), A transitional basalt-pantellerite sequence of fractional crystallization, the Boina Centre (Afar Rift, Ethiopia), Journal of Petrology, 16(1), 22-56.

Barclay, J., M. Carroll, B. Houghton, and C. Wilson (1996), Pre-eruptive volatile content and degassing history of an evolving peralkaline volcano, Journal of Volcanology and Geothermal Research, 74(1-2), 75-87.

Berlo, K., J. Blundy, S. Turner, K. Cashman, C. Hawkesworth, and S. Black (2004), Geochemical precursors to volcanic activity at Mount St. Helens, USA, Science, 306(5699), 1167-1169.

Beutel, E., J. van Wijk, C. Ebinger, D. Keir, and A. Agostini (2010), Formation and stability of magmatic segments in the Main Ethiopian and Afar rifts, Earth and Planetary Science Letters, 293(3-4), 225-235.

Biggs, J., I. Bastow, D. Keir, and E. Lewi (2011), Pulses of deformation reveal frequently recurring shallow magmatic activity beneath the Main Ethiopian Rift, Geochemistry, Geophysics, Geosystems, 12(9).

Biggs, J., S. Ebmeier, W. Aspinall, Z. Lu, M. Pritchard, R. Sparks, and T. Mather (2014a), Global link between deformation and volcanic eruption quantified by satellite imagery, Nature communications, 5, 3471.

Biggs, J., S. Ebmeier, W. Aspinall, Z. Lu, M. Pritchard, R. Sparks, and T. Mather (2014b), Global link between deformation and volcanic eruption quantified by satellite imagery, Nature communications, 5.

1003 Bilham, R., R. Bendick, K. Larson, P. Mohr, J. Braun, S. Tesfaye, and L. Asfaw (1999),
1004 Secular and tidal strain across the Main Ethiopian Rift, Geophysical Research Letters, 26(18),
1005 2789-2792.
1006 Bindeman, I. N., and A. M. Davis (2000), Trace element partitioning between plagioclase
1007 and melt: investigation of dopant influence on partition behavior, Geochimica et
1008 Cosmochimica Acta, 64(16), 2863-2878.
1009 Blundy, J. D., and B. J. Wood (1991), Crystal-chemical controls on the partitioning of Sr and
1010 Ba between plagioclase feldspar, silicate melts, and hydrothermal solutions, Geochimica et
1011 Cosmochimica Acta, 55(1), 193-209.
1012 Borodulin, G., V. Y. Chevychelov, and G. Zaraysky (2009), Experimental study of
1013 partitioning of tantalum, niobium, manganese, and fluorine between aqueous fluoride fluid
1014 and granitic and alkaline melts, paper presented at Doklady Earth Sciences, Springer.
1015 Bougault, H., and R. Hekinian (1974), Rift valley in the Atlantic Ocean near 36° 50′ N:
1016 petrology and geochemistry of basaltic rocks, Earth and Planetary Science Letters, 24(2),
1017 249-261.
1018 Bucholz, C. E., G. A. Gaetani, M. D. Behn, and N. Shimizu (2013), Post-entrapment
1019 modification of volatiles and oxygen fugacity in olivine-hosted melt inclusions, Earth and
1020 Planetary Science Letters.
1021 Caricchi, L., J. Biggs, C. Annen, and S. Ebmeier (2014), The influence of cooling,
1022 crystallisation and re-melting on the interpretation of geodetic signals in volcanic systems,
1023 Earth and Planetary Science Letters, 388, 166-174.
1024 Carroll, M., and J. Webster (Eds.) (1994), Solubilities of sulfur, noble gases, nitrogen,
1025 chlorine, and fluorine in magmas, 231-279. pp.
1026 Carroll, M. R. (2005), Chlorine solubility in evolved alkaline magmas, Annals of
1027 Geophysics, 48(4-5).
1028 Carroll, M. R., and M. J. Rutherford (1987), The stability of igneous anhydrite: experimental
1029 results and implications for sulfur behavior in the 1982 El Chichon trachyandesite and other
1030 evolved magmas, Journal of Petrology, 28(5), 781-801.
1031 Chernet, T., and W. Hart (1999), Petrology and geochemistry of volcanism in the northern
1032 Main Ethiopian Rift-southern Afar transition region, Acta Vulcanologica, 11, 21-42.
1033 Chernet, T., W. K. Hart, J. L. Aronson, and R. C. Walter (1998), New age constraints on the
1034 timing of volcanism and tectonism in the northern Main Ethiopian Rift–southern Afar
1035 transition zone (Ethiopia), Journal of Volcanology and Geothermal Research, 80(3-4), 267-
1036 280.
1037 Cooper, K. M., and A. J. Kent (2014), Rapid remobilization of magmatic crystals kept in cold
1038 storage, Nature.
1039 Corti, G. (2009), Continental rift evolution: from rift initiation to incipient break-up in the
1040 Main Ethiopian Rift, East Africa, Earth-science reviews, 96(1-2), 1-53.
1041 Danyushevsky, L. V., and P. Plechov (2011), Petrolog3: Integrated software for modeling
1042 crystallization processes, Geochemistry, Geophysics, Geosystems, 12(7), Q07021, doi:
1043 10.1029/2011GC003516.
1044 Davidson, J. P., and F. J. Tepley (1997), Recharge in volcanic systems: evidence from
1045 isotope profiles of phenocrysts, Science, 275(5301), 826-829.
1046 Dawson, J., and R. Hinton (2003), Trace-element content and partitioning in calcite, dolomite
1047 and apatite in carbonatite, Phalaborwa, South Africa, Mineralogical Magazine, 67(5), 921-
1048 930.
1049 Di Matteo, V., M. Carroll, H. Behrens, F. Vetere, and R. Brooker (2004), Water solubility in
1050 trachytic melts, Chemical Geology, 213(1-3), 187-196.

1051 Dixon, J. E., L. Leist, C. Langmuir, and J.-G. Schilling (2002), Recycled dehydrated
1052 lithosphere observed in plume-influenced mid-ocean-ridge basalt, Nature, 420(6914), 385-
1053 389.
1054 Ebinger, C., D. Keir, A. Ayele, E. Calais, T. Wright, M. Belachew, J. O. Hammond, E.
1055 Campbell, and W. Buck (2008), Capturing magma intrusion and faulting processes during
1056 continental rupture: seismicity of the Dabbahu (Afar) rift, Geophysical Journal International,
1057 174(3), 1138-1152.
1058 Ewart, A., and W. Griffin (1994), Application of proton-microprobe data to trace-element
1059 partitioning in volcanic rocks, Chemical Geology, 117(1-4), 251-284.
1060 Fedele, L., A. Zanetti, V. Morra, M. Lustrino, L. Melluso, and R. Vannucci (2009),
1061 Clinopyroxene/liquid trace element partitioning in natural trachyte–trachyphonolite systems:
1062 insights from Campi Flegrei (southern Italy), Contr. Mineral. and Petrol., 158(3), 337-356.
1063 Fontijn, K., K. McNamara, A. Z. Tadesse, D. M. Pyle, F. Dessalegn, W. Hutchison, T. A.
1064 Mather, and G. Yirgu (2018), Contrasting styles of post-caldera volcanism along the Main
1065 Ethiopian Rift: Implications for contemporary volcanic hazards, Journal of Volcanology and
1066 Geothermal Research, 356, 90-113.
1067 Fortin, M.-A., J. Riddle, Y. Desjardins-Langlais, and D. R. Baker (2015), The effect of water
1068 on the sulfur concentration at sulfide saturation (SCSS) in natural melts, Geochimica et
1069 Cosmochimica Acta, 160, 100-116.
1070 Fujimaki, H. (1986), Partition coefficients of Hf, Zr, and REE between zircon, apatite, and
1071 liquid, Contr. Mineral. and Petrol., 94(1), 42-45.
1072 Fusillo, R. (2018), Understanding the volcanic history of Corbetti caldera (Main Ethiopian
1073 Rift): An integrated study of the stratigraphic reconstruction and the geochemical
1074 characterization of the deposits., Masters thesis.
1075 Gaetani, G. A., and T. L. Grove (1995), Partitioning of rare earth elements between
1076 clinopyroxene and silicate melt Crystal-chemical controls, Geochimica et Cosmochimica
1077 Acta, 59(10), 1951-1962.
1078 Gaillard, F., and G. I. Marziano (2005), Electrical conductivity of magma in the course of
1079 crystallization controlled by their residual liquid composition, Journal of Geophysical
1080 Research: Solid Earth, 110(B6).
1081 Gerlach, T. M., H. R. Westrich, and R. B. Symonds (1996), Preeruption vapor in magma of
1082 the climactic Mount Pinatubo eruption: Source of the giant stratospheric sulfur dioxide cloud,
1083 Fire and mud: eruptions and lahars of Mount Pinatubo, Philippines, 415, 33.
1084 Ghiorso, M. S., and G. A. Gualda (2015), An H 2 O–CO 2 mixed fluid saturation model
1085 compatible with rhyolite-MELTS, Contr. Mineral. and Petrol., 169(6), 53.
1086 Gioncada, A., and P. Landi (2010), The pre-eruptive volatile contents of recent basaltic and
1087 pantelleritic magmas at Pantelleria (Italy), Journal of Volcanology and Geothermal Research,
1088 189(1-2), 191-201.
1089 Gleeson, M. L., M. J. Stock, D. M. Pyle, T. A. Mather, W. Hutchison, G. Yirgu, and J. Wade
1090 (2017), Constraining magma storage conditions at a restless volcano in the Main Ethiopian
1091 Rift using phase equilibria models, Journal of Volcanology and Geothermal Research, 337,
1092 44-61.
1093 Gottsmann, J., and M. Battaglia (2008), Deciphering causes of unrest at explosive collapse
1094 calderas: recent advances and future challenges of joint time-lapse gravimetric and ground
1095 deformation studies, Developments in Volcanology, 10, 417-446.
1096 Green, T., J. Adam, and S. Site (1993), Proton microprobe determined trace element partition
1097 coefficients between pargasite, augite and silicate or carbonatitic melts, EOS (American
1098 Geophysical Union Transactions), 74, 340.

Gudmundsson, A. (2005), The effects of layering and local stresses in composite volcanoes on dyke emplacement and volcanic hazards, Comptes Rendus Geoscience, 337(13), 1216-1222.
Harris, W. C. (1844), The Highlands of Aethiopia: In Three Volumes, Longman, Brown, Green and Longmans.
Hartley, M. E., J. Maclennan, M. Edmonds, and T. Thordarson (2014), Reconstructing the deep CO< sub> 2</sub> degassing behaviour of large basaltic fissure eruptions, Earth and Planetary Science Letters, 393, 120-131.
Hauri, E. H., E. Cottrell, K. A. Kelley, J. M. Tucker, K. Shimizu, M. Le Voyer, J. Marske, and A. E. Saal (2019), Carbon in the Convecting Mantle, in Earth's Deep Carbon: past to present, edited, Cambridge University Press.
Henderson, C., and W. Pierozynski (2012), An experimental study of Sr, Ba and Rb partitioning between alkali feldspar and silicate liquid in the system nepheline-kalsilite-quartz at 0.1 GPa P (H2O): a revisitation and reassessment, Mineralogical Magazine, 76(1), 157-190.
Hill, E., B. J. Wood, and J. D. Blundy (2000), The effect of Ca-Tschermaks component on trace element partitioning between clinopyroxene and silicate melt, Lithos, 53(3-4), 203-215.
Hübert, J., K. Whaler, and S. Fisseha (2018), The Electrical Structure of the Central Main Ethiopian Rift as Imaged by Magnetotellurics: Implications for Magma Storage and Pathways, Journal of Geophysical Research: Solid Earth, 123(7), 6019-6032.
Hunt, J. A., T. A. Mather, and D. M. Pyle (2020), Morphological comparison of distributed volcanic fields in the Main Ethiopian Rift using high-resolution digital elevation models, Journal of Volcanology and Geothermal Research, 393, 106732.
Hunt, J. A., A. Zafu, T. A. Mather, D. M. Pyle, and P. H. Barry (2017), Spatially Variable CO2 Degassing in the Main Ethiopian Rift: Implications for Magma Storage, Volatile Transport, and Rift-Related Emissions, Geochemistry, Geophysics, Geosystems, 18(10), 3714-3737.
Huppert, H. E., and A. W. Woods (2002), The role of volatiles in magma chamber dynamics, Nature, 420(6915), 493-495.
Hutchison, W. (2015), Past, present and future volcanic activity at restless calderas in the Main Ethiopian Rift, University of Oxford.
Hutchison, W., T. A. Mather, D. M. Pyle, J. Biggs, and G. Yirgu (2015), Structural controls on fluid pathways in an active rift system: A case study of the Aluto volcanic complex, Geosphere, 11(3), 542-562.
Hutchison, W., J. Biggs, T. A. Mather, D. M. Pyle, E. Lewi, G. Yirgu, S. Caliro, G. Chiodini, L. E. Clor, and T. P. Fischer (2016a), Causes of unrest at silicic calderas in the East African Rift: New constraints from InSAR and soil-gas chemistry at Aluto volcano, Ethiopia, Geochemistry, Geophysics, Geosystems, 17(8), 3008-3030.
Hutchison, W., R. Fusillo, D. M. Pyle, T. A. Mather, J. D. Blundy, J. Biggs, G. Yirgu, B. E. Cohen, R. A. Brooker, and D. N. Barfod (2016b), A pulse of mid-Pleistocene rift volcanism in Ethiopia at the dawn of modern humans, Nature Communications, 7, 13192.
Hutchison, W., T. A. Mather, D. M. Pyle, A. J. Boyce, M. L. Gleeson, G. Yirgu, J. D. Blundy, D. J. Ferguson, C. Vye-Brown, and I. L. Millar (2018), The evolution of magma during continental rifting: New constraints from the isotopic and trace element signatures of silicic magmas from Ethiopian volcanoes, Earth and Planetary Science Letters, 489, 203-218.
Iddon, F., C. Jackson, W. Hutchison, K. Fontijn, D. M. Pyle, T. A. Mather, G. Yirgu, and M. Edmonds (2019), Mixing and crystal scavenging in the Main Ethiopian Rift revealed by trace element systematics in feldspars and glasses, Geochemistry, Geophysics, Geosystems, 20(1), 230-259.

Iveson, A. A., J. D. Webster, M. C. Rowe, and O. K. Neill (2017), Major Element and Halogen (F, Cl) Mineral–Melt–Fluid Partitioning in Hydrous Rhyodacitic Melts at Shallow Crustal Conditions, Journal of Petrology, 58(12), 2465-2492.
Johnson, D. J. (1992), Dynamics of magma storage in the summit reservoir of Kilauea volcano, Hawaii, Journal of Geophysical Research: Solid Earth (1978–2012), 97(B2), 1807-1820.
Johnson, N., K. Whaler, S. Hautot, S. Fisseha, M. Desissa, and G. Dawes (2016), Magma imaged magnetotellurically beneath an active and an inactive magmatic segment in Afar, Ethiopia, Geological Society, London, Special Publications, 420(1), 105-125.
Jugo, P. J. (2009), Sulfur content at sulfide saturation in oxidized magmas, Geology, 37(5), 415-418.
Jugo, P. J., M. Wilke, and R. E. Botcharnikov (2010), Sulfur K-edge XANES analysis of natural and synthetic basaltic glasses: Implications for S speciation and S content as function of oxygen fugacity, Geochimica et Cosmochimica Acta, 74(20), 5926-5938.
Keir, D., C. Ebinger, G. Stuart, E. Daly, and A. Ayele (2006), Strain accommodation by magmatism and faulting as rifting proceeds to breakup: Seismicity of the northern Ethiopian rift, Journal of Geophysical Research: Solid Earth, 111(B5).
Kendrick, M., C. Hémond, V. Kamenetsky, L. Danyushevsky, C. W. Devey, T. Rodemann, M. Jackson, and M. Perfit (2017), Seawater cycled throughout Earth's mantle in partially serpentinized lithosphere, Nature Geoscience, 10(3), 222.
Kent, A. J. R. (2008), Melt Inclusions in Basaltic and Related Volcanic Rocks, Reviews in Mineralogy and Geochemistry, 69(1), 273-331, doi: 10.2138/rmg.2008.69.8.
Kent, A. J. R., J. Blundy, K. V. Cashman, K. M. Cooper, C. Donnelly, J. S. Pallister, M. Reagan, M. C. Rowe, and C. R. Thornber (2007), Vapor transfer prior to the October 2004 eruption of Mount St. Helens, Washington, Geology, 35(3), 231-234, doi: 10.1130/g22809a.1.
Keranen, K., S. Klemperer, R. Gloaguen, and E. W. Group (2004), Three-dimensional seismic imaging of a protoridge axis in the Main Ethiopian rift, Geology, 32(11), 949-952.
Kilinc, I., and C. Burnham (1972), Partitioning of chloride between a silicate melt and coexisting aqueous phase from 2 to 8 kilobars, Economic Geology, 67(2), 231-235.
Kim, S., A. A. Nyblade, J. Rhie, C.-E. Baag, and T.-S. Kang (2012), Crustal S-wave velocity structure of the Main Ethiopian Rift from ambient noise tomography, Geophysical Journal International, 191(2), 865-878.
Klemme, S., and C. Dalpé (2003), Trace-element partitioning between apatite and carbonatite melt, American Mineralogist, 88(4), 639-646.
Koga, K., N. Cluzel, E. Rose-Koga, D. Laporte, and N. Shimizu (2008), Experimental demonstration of lithium-boron depletion during magma degassing, paper presented at AGU Fall Meeting Abstracts.
Kutterolf, S., T. H. Hansteen, K. Appel, A. Freundt, K. Krüger, W. Perez, and H. Wehrmann (2013), Combined bromine and chlorine release from large explosive volcanic eruptions: A threat to stratospheric ozone?, Geology, 41(6), 707-710.
Lanzo, G., P. Landi, and S. G. Rotolo (2013), Volatiles in pantellerite magmas: a case study of the Green Tuff Plinian eruption (Island of Pantelleria, Italy), Journal of volcanology and geothermal research, 262, 153-163.
Larsen, L. M. (1979), Distribution of REE and other trace elements between phenocrysts and peralkaline undersaturated magmas, exemplified by rocks from the Gardar igneous province, south Greenland, Lithos, 12(4), 303-315.
Laumonier, M., F. Gaillard, D. Muir, J. Blundy, and M. Unsworth (2017), Giant magmatic water reservoirs at mid-crustal depth inferred from electrical conductivity and the growth of the continental crust, Earth and Planetary Science Letters, 457, 173-180.

Le Voyer, M., K. A. Kelley, E. Cottrell, and E. Hauri (2017), Heterogeneity in mantle carbon content from CO 2-undersaturated basalts, Nature Communications, 8, 14062.
Lee, H., J. D. Muirhead, T. P. Fischer, C. J. Ebinger, S. A. Kattenhorn, Z. D. Sharp, and G. Kianji (2016), Massive and prolonged deep carbon emissions associated with continental rifting, Nature Geoscience.
Lemarchand, F., B. Villemant, and G. Calas (1987), Trace element distribution coefficients in alkaline series, Geochimica et Cosmochimica Acta, 51(5), 1071-1081.
Li, C., E. M. Ripley, and A. J. Naldrett (2009), A new genetic model for the giant Ni-Cu-PGE sulfide deposits associated with the Siberian flood basalts, Economic Geology, 104(2), 291-301.
Lloyd, R., J. Biggs, M. Wilks, A. Nowacki, J.-M. Kendall, A. Ayele, E. Lewi, and H. Eysteinsson (2018), Evidence for cross rift structural controls on deformation and seismicity at a continental rift caldera, Earth and Planetary Science Letters, 487, 190-200.
Lowenstern, J. B. (1995), Applications of silicate-melt inclusions to the study of magmatic volatiles, Magmas, fluids, and ore deposits, 23, 71-99.
Luhr, J. F., I. S. Carmichael, and J. C. Varekamp (1984), The 1982 eruptions of El Chichón Volcano, Chiapas, Mexico: mineralogy and petrology of the anhydritebearing pumices, Journal of Volcanology and Geothermal Research, 23(1-2), 69-108.
Lukanin, O. (2015), Chlorine partitioning between melt and aqueous chloride fluid during granite magma. Degassing I. Decompression-induced melt degassing, Geochemistry International, 53(9), 786-810.
Lukanin, O. (2016), Chlorine partitioning between melt and aqueous chloride fluid phase during granite magma degassing. Part II. Crystallization-induced degassing of melts, Geochemistry International, 54(8), 660-680.
Macdonald, R. (1974), Nomenclature and petrochemistry of the peralkaline oversaturated extrusive rocks, Bulletin volcanologique, 38(2), 498-516.
Macdonald, R., and B. Bagiński (2009), The central Kenya peralkaline province: a unique assemblage of magmatic systems, Mineralogical Magazine, 73(1), 1-16.
Macdonald, R., B. Bagiński, F. Ronga, P. Dzierżanowski, M. Lustrino, A. Marzoli, and L. Melluso (2012), Evidence for extreme fractionation of peralkaline silicic magmas, the Boseti volcanic complex, Main Ethiopian Rift, Mineralogy and Petrology, 104(3-4), 163-175.
Maclennan, J., D. McKenzie, K. Gronvöld, and L. Slater (2001), Crustal accretion under northern Iceland, Earth and Planetary Science Letters, 191(3), 295-310.
Mahood, G. A., and J. A. Stimac (1990), Trace-element partitioning in pantellerites and trachytes, Geochimica et Cosmochimica Acta, 54(8), 2257-2276.
Marks, M., R. Halama, T. Wenzel, and G. Markl (2004), Trace element variations in clinopyroxene and amphibole from alkaline to peralkaline syenites and granites: implications for mineral–melt trace-element partitioning, Chemical geology, 211(3-4), 185-215.
Martini, M. (1984), On the behaviour of fluorine in volcanic processes, Bulletin Volcanologique, 47(3), 483-489.
Mathez, E. A., and J. D. Webster (2005), Partitioning behavior of chlorine and fluorine in the system apatite-silicate melt-fluid, Geochimica et Cosmochimica Acta, 69(5), 1275-1286.
Mavrogenes, J. A., and H. S. C. O'Neill (1999), The relative effects of pressure, temperature and oxygen fugacity on the solubility of sulfide in mafic magmas, Geochimica et Cosmochimica Acta, 63(7), 1173-1180.
McCormick Kilbride, B., M. Edmonds, and J. Biggs (2016), Observing eruptions of gas-rich compressible magmas from space, Nature Communications, 7.
McCubbin, F. M., K. E. Vander Kaaden, R. Tartèse, J. W. Boyce, S. Mikhail, E. S. Whitson, A. S. Bell, M. Anand, I. A. Franchi, and J. Wang (2015), Experimental investigation of F, Cl,

and OH partitioning between apatite and Fe-rich basaltic melt at 1.0–1.2 GPa and 950–1000 C, American Mineralogist, 100(8-9), 1790-1802.
Métrich, N., A. Bertagnini, P. Landi, and M. Rosi (2001), Crystallization driven by decompression and water loss at Stromboli volcano (Aeolian Islands, Italy), Journal of Petrology, 42(8), 1471-1490.
Michael, P. (1995), Regionally distinctive sources of depleted MORB: Evidence from trace elements and H2O, Earth and Planetary Science Letters, 131(3-4), 301-320.
Mickus, K., K. Tadesse, G. Keller, and B. Oluma (2007), Gravity analysis of the main Ethiopian rift, Journal of African Earth Sciences, 48(2-3), 59-69.
Mohr, P. (1983), Perspectives on the Ethiopian volcanic province, Bulletin volcanologique, 46(1), 23-43.
Moore, L. R., E. Gazel, R. Tuohy, A. S. Lloyd, R. Esposito, M. Steele-MacInnis, E. H. Hauri, P. J. Wallace, T. Plank, and R. J. J. A. M. Bodnar (2015), Bubbles matter: An assessment of the contribution of vapor bubbles to melt inclusion volatile budgets, 100(4), 806-823.
Nagasawa, H. (1970), Rare earth concentrations in zircons and apatites and their host dacites and granites, Earth and Planetary Science Letters, 9(4), 359-364.
Nagasawa, H., and C. C. Schnetzler (1971), Partitioning of rare earth, alkali and alkaline earth elements between phenocrysts and acidic igneous magma, Geochimica et Cosmochimica Acta, 35(9), 953-968.
Neave, D. A., and K. D. Putirka (2017), A new clinopyroxene-liquid barometer, and implications for magma storage pressures under Icelandic rift zones, American Mineralogist, 102(4), 777-794.
Neave, D. A., G. Fabbro, R. A. Herd, C. M. Petrone, and M. Edmonds (2012), Melting, differentiation and degassing at the Pantelleria volcano, Italy, Journal of Petrology, 53(3), 637-663.
Neuberg, J., and C. O'Gorman (2002), A model of the seismic wavefield in gas-charged magma: application to Soufriere Hills Volcano, Montserrat, Geological Society, London, Memoirs, 21(1), 603-609.
Nikogosian, I., and A. Sobolev (1997), Ion-microprobe analysis of melt Inclusions in olivine: experience in estimating the olivine-melt partition coefficients of trace elements, Geochemistry International, 35(2), 119-126.
Nimis, P., and P. Ulmer (1998), Clinopyroxene geobarometry of magmatic rocks Part 1: An expanded structural geobarometer for anhydrous and hydrous, basic and ultrabasic systems, Contr. Mineral. and Petrol., 133(1-2), 122-135.
Oppenheimer, C. (2003), Climatic, environmental and human consequences of the largest known historic eruption: Tambora volcano (Indonesia) 1815, Progress in physical geography, 27(2), 230-259.
Papale, P. (1999), Modeling of the solubility of a two-component H ₂ O+CO ₂ fluid in silicate liquids, American Mineralogist, 84(4), 477-492, doi: 10.2138/am-1999-0402.
Parat, F., and F. Holtz (2004), Sulfur partitioning between apatite and melt and effect of sulfur on apatite solubility at oxidizing conditions, Contr. Mineral. and Petrol., 147(2), 201-212.
Paster, T. P., D. S. Schauwecker, and L. A. Haskin (1974), The behavior of some trace elements during solidification of the Skaergaard layered series, Geochimica et Cosmochimica Acta, 38(10), 1549-1577.
Peccerillo, A., B. Mandefro, G. Solomon, H. Bedru, and K. Tesfaye (1998), The Precambrian rocks from Southern Ethiopia: petrology, geochemistry and their interaction with the recent volcanism from the Ethiopian Rift Valley, Neues Jahrbuch für Mineralogie-Abhandlungen, 237-262.

1297 Peccerillo, A., M. Barberio, G. Yirgu, D. Ayalew, M. Barbieri, and T. Wu (2003),
1298 Relationships between mafic and peralkaline silicic magmatism in continental rift settings: a
1299 petrological, geochemical and isotopic study of the Gedemsa volcano, central Ethiopian rift,
1300 Journal of Petrology, 44(11), 2003-2032.
1301 Putirka, K. D. (2005), Igneous thermometers and barometers based on plagioclase+ liquid
1302 equilibria: Tests of some existing models and new calibrations, American Mineralogist, 90(2-
1303 3), 336-346.
1304 Rampey, M. L. (2005), The geology of the Kone volcanic complex, Ethiopia, University of
1305 Cambridge.
1306 Rivalta, E., and P. Segall (2008), Magma compressibility and the missing source for some
1307 dike intrusions, Geophysical Research Letters, 35(4), L04306, doi: 10.1029/2007GL032521.
1308 Roeder, P. L., and R. F. Emslie (1970), Olivine-liquid equilibrium, Contr. Mineral. and
1309 Petrol., 29(4), 275-289, doi: 10.1007/BF00371276.
1310 Rooney, T., T. Furman, I. Bastow, D. Ayalew, and G. Yirgu (2007), Lithospheric
1311 modification during crustal extension in the Main Ethiopian Rift, Journal of Geophysical
1312 Research: Solid Earth, 112(B10).
1313 Rooney, T. O., I. D. Bastow, and D. Keir (2011), Insights into extensional processes during
1314 magma assisted rifting: Evidence from aligned scoria cones, Journal of Volcanology and
1315 Geothermal Research, 201(1-4), 83-96.
1316 Rooney, T. O., T. Furman, G. Yirgu, and D. Ayalew (2005), Structure of the Ethiopian
1317 lithosphere: Xenolith evidence in the Main Ethiopian Rift, Geochimica et Cosmochimica
1318 Acta, 69(15), 3889-3910.
1319 Rooney, T. O., W. K. Hart, C. M. Hall, D. Ayalew, M. S. Ghiorso, P. Hidalgo, and G. Yirgu
1320 (2012), Peralkaline magma evolution and the tephra record in the Ethiopian Rift, Contr.
1321 Mineral. and Petrol., 164(3), 407-426.
1322 Rosenthal, A., E. Hauri, and M. Hirschmann (2015), Experimental determination of C, F, and
1323 H partitioning between mantle minerals and carbonated basalt, CO 2/Ba and CO 2/Nb
1324 systematics of partial melting, and the CO 2 contents of basaltic source regions, Earth and
1325 Planetary Science Letters, 412, 77-87.
1326 Saal, A. E., E. H. Hauri, C. H. Langmuir, and M. R. Perfit (2002), Vapour undersaturation in
1327 primitive mid-ocean-ridge basalt and the volatile content of Earth's upper mantle, Nature,
1328 419(6906), 451-455, doi:
1329 http://www.nature.com/nature/journal/v419/n6906/suppinfo/nature01073_S1.html.
1330 Samrock, F., A. Kuvshinov, J. Bakker, A. Jackson, and S. Fisseha (2015), 3-D analysis and
1331 interpretation of magnetotelluric data from the Aluto-Langano geothermal field, Ethiopia,
1332 Geophysical Journal International, 202(3), 1923-1948.
1333 Saria, E., E. Calais, D. Stamps, D. Delvaux, and C. Hartnady (2014), Present- day kinematics
1334 of the East African Rift, Journal of Geophysical Research: Solid Earth, 119(4), 3584-3600.
1335 Scaillet, B., and R. Macdonald (2006), Experimental and thermodynamic constraints on the
1336 sulphur yield of peralkaline and metaluminous silicic flood eruptions, Journal of Petrology,
1337 47(7), 1413-1437.
1338 Segall, P. (2013), Volcano deformation and eruption forecasting, Geological Society,
1339 London, Special Publications, 380(1), 85-106.
1340 Shand, S. (1927), On the relations between silica, alumina, and the bases in eruptive rocks,
1341 considered as a means of classification, Geological Magazine, 64(10), 446-449.
1342 Shinohara, H. (1994), Exsolution of immiscible vapor and liquid phases from a crystallizing
1343 silicate melt: Implications for chlorine and metal transport, Geochimica et Cosmochimica
1344 Acta, 58(23), 5215-5221.

1345 Shishkina, T., R. Botcharnikov, F. Holtz, R. Almeev, and M. V. Portnyagin (2010), Solubility
1346 of H2O-and CO2-bearing fluids in tholeiitic basalts at pressures up to 500 MPa, Chemical
1347 geology, 277(1-2), 115-125.
1348 Shishkina, T. A., R. E. Botcharnikov, F. Holtz, R. R. Almeev, A. M. Jazwa, and A. A.
1349 Jakubiak (2014), Compositional and pressure effects on the solubility of H2O and CO2 in
1350 mafic melts, Chemical Geology, 388, 112-129.
1351 Signorelli, S., and M. Carroll (2002), Experimental study of Cl solubility in hydrous alkaline
1352 melts: constraints on the theoretical maximum amount of Cl in trachytic and phonolitic melts,
1353 Contr. Mineral. and Petrol., 143(2), 209-218.
1354 Signorelli, S., G. Vaggelli, C. Romano, and M. Carroll (2001), Volatile element zonation in
1355 Campanian Ignimbrite magmas (Phlegrean Fields, Italy): evidence from the study of glass
1356 inclusions and matrix glasses, Contr. Mineral. and Petrol., 140(5), 543-553.
1357 Sigurdsson, H., and S. Carey (1992), The eruption of Tambora in 1815: Environmental
1358 effects and eruption dynamics, The Year Without a Summer, 16-45.
1359 Sobolev, A. (1996), Melt inclusions in minerals as a source of principle petrological
1360 information, Petrology, 4(3), 209-220.
1361 Steele-Macinnis, M., R. Esposito, and R. J. Bodnar (2011), Thermodynamic model for the
1362 effect of post-entrapment crystallization on the H2O–CO2 systematics of vapor-saturated,
1363 silicate melt inclusions, Journal of Petrology, 52(12), 2461-2482, doi:
1364 10.1093/petrology/egr052.
1365 Stix, J., and M. P. Gorton (1990), Variations in trace element partition coefficients in
1366 sanidine in the Cerro Toledo Rhyolite, Jemez Mountains, New Mexico: Effects of
1367 composition, temperature, and volatiles, Geochimica et Cosmochimica Acta, 54(10), 2697-
1368 2708.
1369 Tait, S., C. Jaupart, and S. Vergniolle (1989), Pressure, gas content and eruption periodicity
1370 of a shallow, crystallising magma chamber, Earth and Planetary Science Letters, 92(1), 107-
1371 123, doi: http://dx.doi.org/10.1016/0012-821X(89)90025-3.
1372 Taylor Jr, H. P. (1980), The effects of assimilation of country rocks by magmas on 18O/16O
1373 and 87Sr/86Sr systematics in igneous rocks, Earth and Planetary Science Letters, 47(2), 243-
1374 254.
1375 Tepley, F., J. Davidson, R. Tilling, and J. G. Arth (2000), Magma mixing, recharge and
1376 eruption histories recorded in plagioclase phenocrysts from El Chichon Volcano, Mexico,
1377 Journal of Petrology, 41(9), 1397-1411.
1378 Trua, T., C. Deniel, and R. Mazzuoli (1999), Crustal control in the genesis of Plio-Quaternary
1379 bimodal magmatism of the Main Ethiopian Rift (MER): geochemical and isotopic (Sr, Nd,
1380 Pb) evidence, Chemical Geology, 155(3-4), 201-231.
1381 Villemant, B. (1988), Trace element evolution in the Phlegrean Fields (Central Italy):
1382 fractional crystallization and selective enrichment, Contr. Mineral. and Petrol., 98(2), 169-
1383 183.
1384 Villemant, B., H. Jaffrezic, J.-L. Joron, and M. Treuil (1981), Distribution coefficients of
1385 major and trace elements; fractional crystallization in the alkali basalt series of Chaine des
1386 Puys (Massif Central, France), Geochimica et Cosmochimica Acta, 45(11), 1997-2016.
1387 Wallace, P. J., and T. M. Gerlach (1994), Magmatic vapor source for sulfur dioxide released
1388 during volcanic eruptions: evidence from Mount Pinatubo, Science, 265(5171), 497-499.
1389 Webster, J., J. Holloway, and R. Hervig (1989), Partitioning of lithophile trace elements
1390 between H 2 O and H 2 O+ CO 2 fluids and topaz rhyolite melt, Economic Geology, 84(1),
1391 116-134.
1392 Webster, J. D., C. M. Tappen, and C. W. Mandeville (2009), Partitioning behavior of
1393 chlorine and fluorine in the system apatite–melt–fluid. II: Felsic silicate systems at 200 MPa,
1394 Geochimica et Cosmochimica Acta, 73(3), 559-581.

1395 Webster, J. D., B. A. Goldoff, R. N. Flesch, P. A. Nadeau, and Z. W. Silbert (2017),
1396 Hydroxyl, Cl, and F partitioning between high-silica rhyolitic melts-apatite-fluid (s) at 50–
1397 200 MPa and 700–1000 C, American Mineralogist, 102(1), 61-74.
1398 Webster, J. D., F. Vetere, R. E. Botcharnikov, B. Goldoff, A. McBirney, and A. L. Doherty
1399 (2015), Experimental and modeled chlorine solubilities in aluminosilicate melts at 1 to 7000
1400 bars and 700 to 1250 C: Applications to magmas of Augustine Volcano, Alaska, American
1401 Mineralogist, 100(2-3), 522-535.
1402 White, J. C., D. F. Parker, and M. Ren (2009), The origin of trachyte and pantellerite from
1403 Pantelleria, Italy: insights from major element, trace element, and thermodynamic modelling,
1404 Journal of Volcanology and Geothermal Research, 179(1-2), 33-55.
1405 Wilks, M., J.-M. Kendall, A. Nowacki, J. Biggs, J. Wookey, Y. Birhanu, A. Ayele, and T.
1406 Bedada (2017), Seismicity associated with magmatism, faulting and hydrothermal circulation
1407 at Aluto Volcano, Main Ethiopian Rift, Journal of Volcanology and Geothermal Research,
1408 340, 52-67.
1409 Woldegabriel, G., J. L. Aronson, and R. C. Walter (1990), Geology, geochronology, and rift
1410 basin development in the central sector of the Main Ethiopia Rift, Geological Society of
1411 America Bulletin, 102(4), 439-458.
1412 Wood, B. J., and R. Trigila (2001), Experimental determination of aluminous clinopyroxene–
1413 melt partition coefficients for potassic liquids, with application to the evolution of the Roman
1414 province potassic magmas, Chemical Geology, 172(3-4), 213-223.
1415

Figure 1.

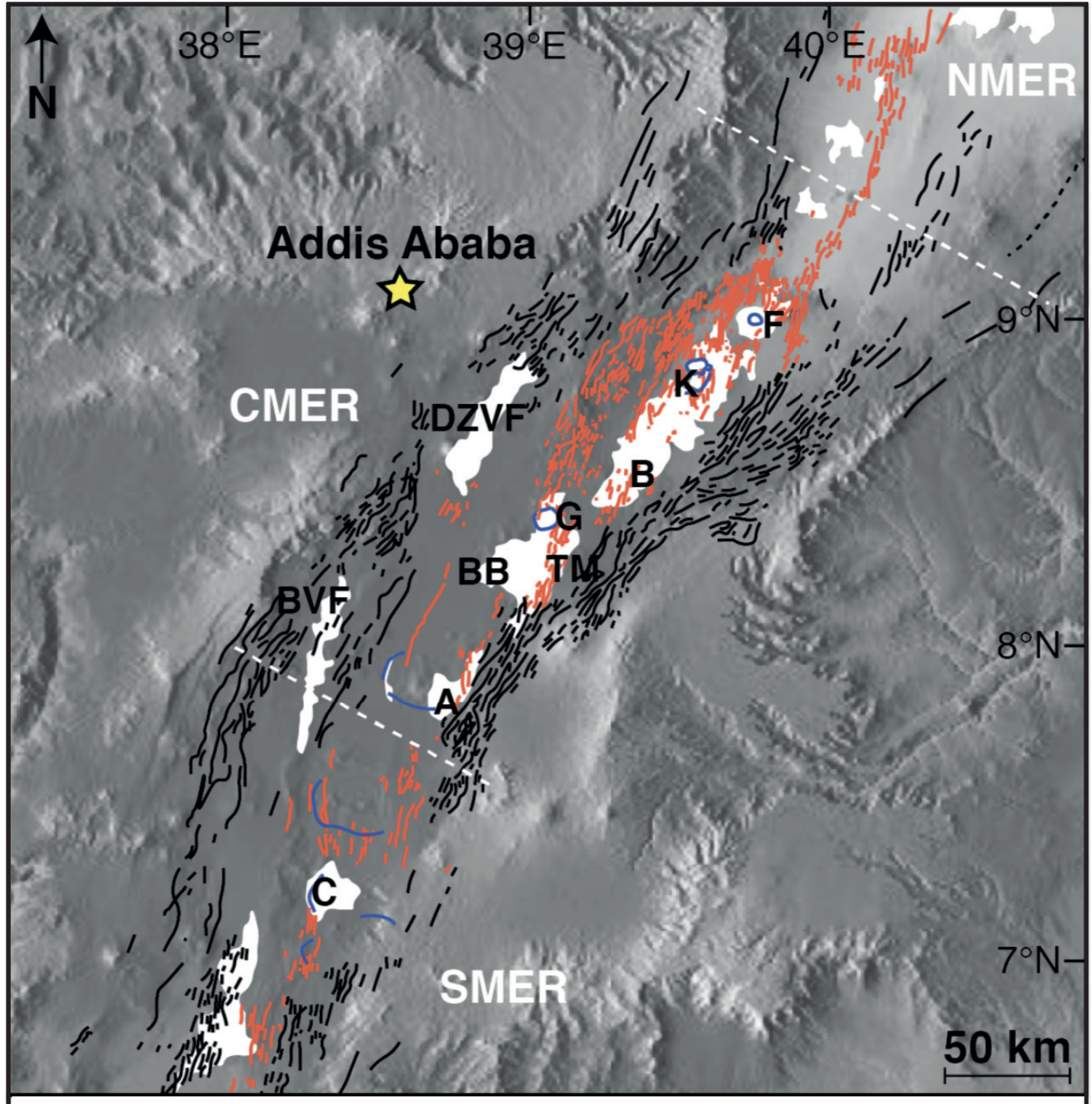

Boundary fault — Wonji fault belt — Caldera margin

Quaternary eruption deposits

C-Corbetti; **A**-Aluto; **BVF**- Butajira volcanic field; **BB**-Bora-Baricha; **TM**-Tullu Moye; **G**-Gedemsa; **DZVF**- Debre Zeit volcanic field; **B**-Boset-Bericha; **K**-Kone; **F**-Fentale

Figure 2.

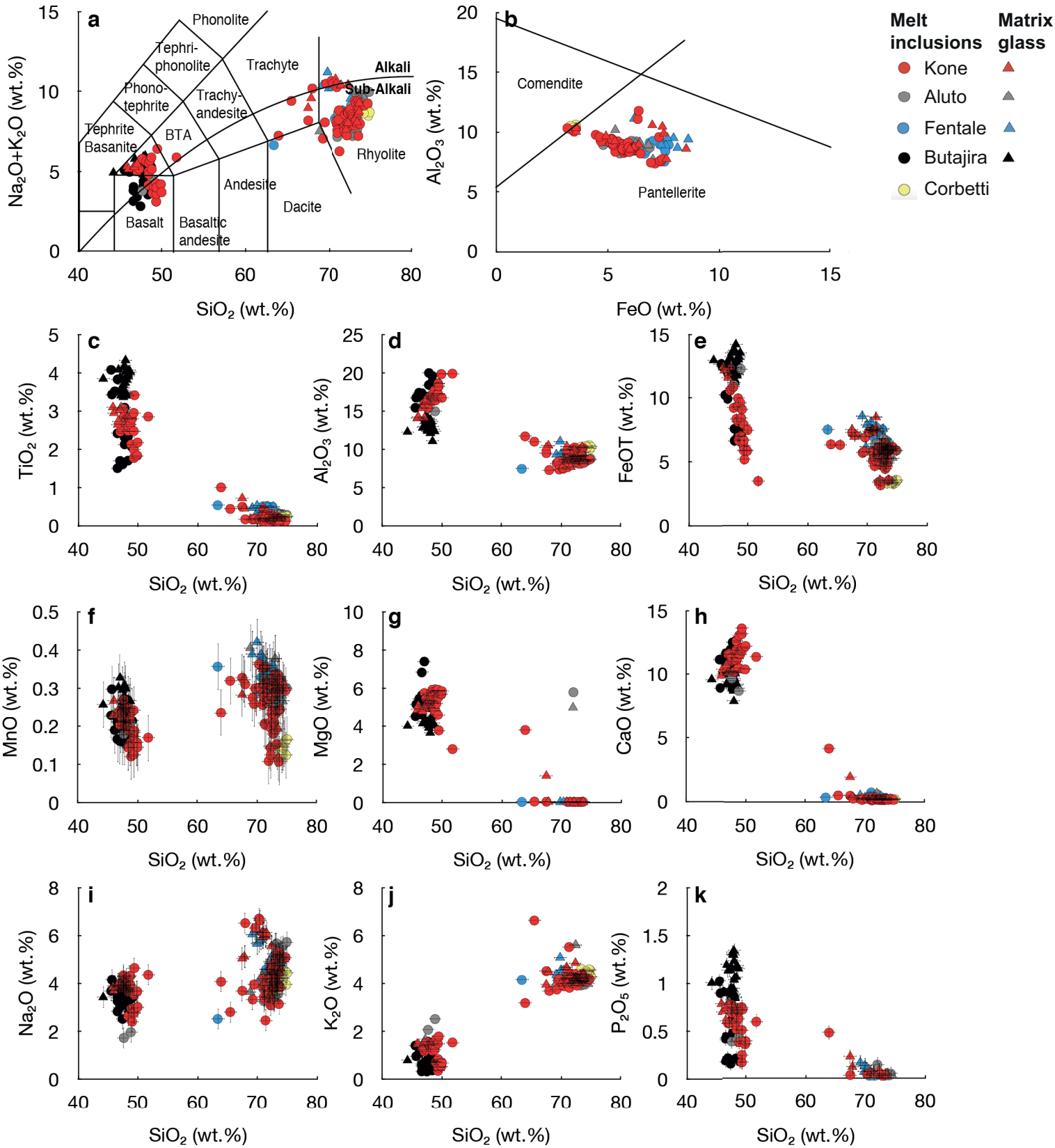
a
Phonolite
Tephri-phonolite
Trachyte
Alkali
Sub-Alkali
Phono-tephrite
Trachy-andesite
Tephrite Basanite
BTA
Rhyolite
Andesite
Dacite
Basalt
Basaltic andesite
Na2O+K2O (wt.%)
SiO2 (wt.%)
b
Comendite
Pantellerite
Al2O3 (wt.%)
FeO (wt.%)
Melt inclusions
Matrix glass
Kone
Aluto
Fentale
Butajira
Corbetti
c
TiO2 (wt.%)
d
Al2O3 (wt.%)
e
FeOT (wt.%)
f
MnO (wt.%)
g
MgO (wt.%)
h
CaO (wt.%)
i
Na2O (wt.%)
j
K2O (wt.%)
k
P2O5 (wt.%)

Figure 3.

a
Rb (ppm)
Zr (ppm)
b
Ba (ppm)
Zr (ppm)
c
La (ppm)
Zr (ppm)
d
Ce (ppm)
Zr (ppm)
e
Pr (ppm)
Zr (ppm)
f
Sr (ppm)
Zr (ppm)
g
Yb (ppm)
Zr (ppm)
h
Lu (ppm)
Zr (ppm)
i
Rb/Nb (ppm)
Rb (ppm)
Ethiopian Precambrian basement
(Peccerillo et al., 1998)

Melt inclusions / **Matrix glass**

- Kone
- Aluto
- Fentale
- Butajira
- Corbetti

Rhyolite-Melts fractional crystallisation models

- Mafic
- Intermediate
- Trachytic
- Pantelleritic
- \+ Feldspar assimilation

Figure 4.

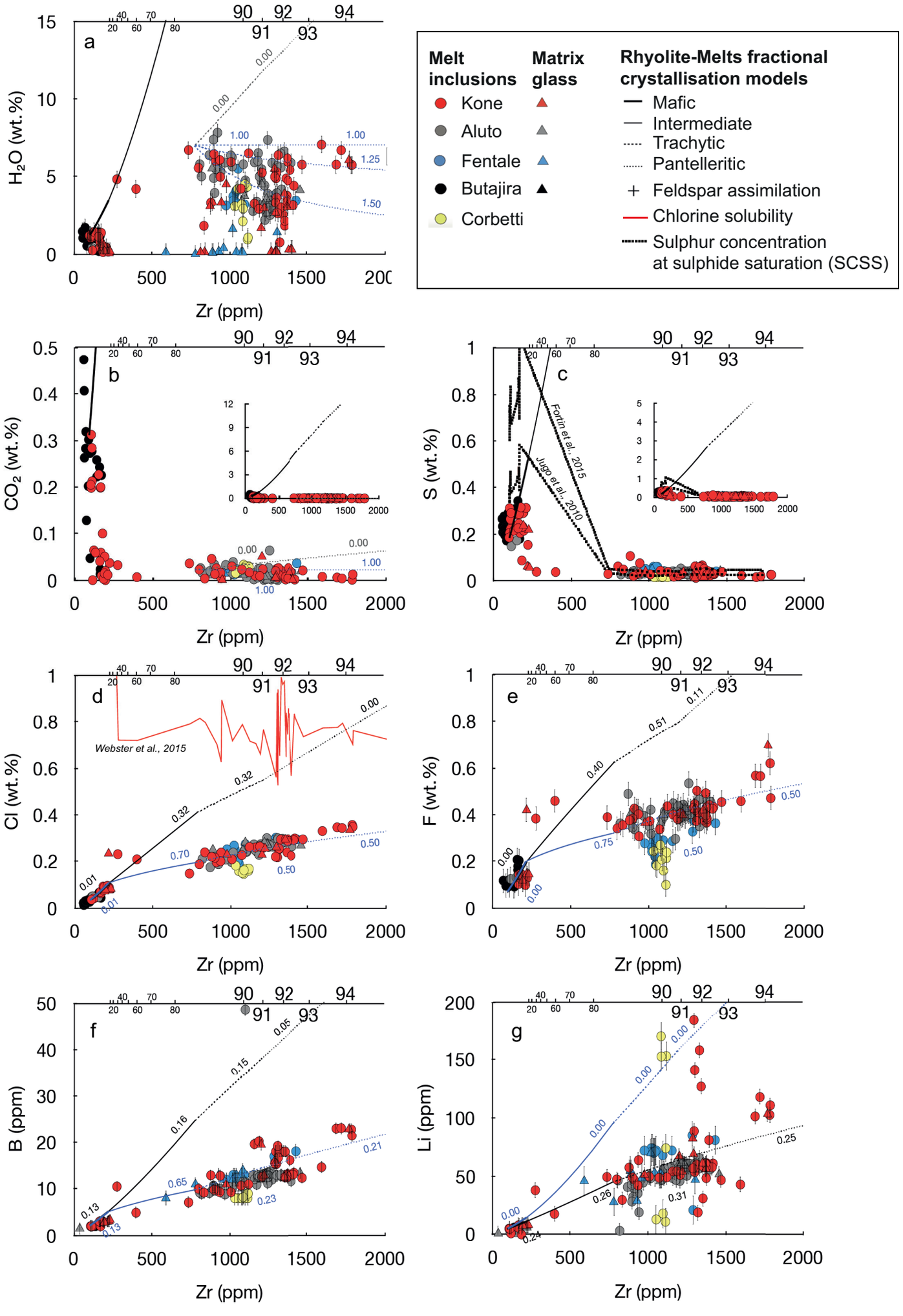
Melt inclusions
Kone
Aluto
Fentale
Butajira
Corbetti
Matrix glass
Rhyolite-Melts fractional crystallisation models
Mafic
Intermediate
Trachytic
Pantelleritic
Feldspar assimilation
Chlorine solubility
Sulphur concentration at sulphide saturation (SCSS)
a
b
c
d
e
f
g
H2O (wt.%)
CO2 (wt.%)
S (wt.%)
Cl (wt.%)
F (wt.%)
B (ppm)
Li (ppm)
Zr (ppm)
Fortin et al., 2015
Jugo et al., 2010
Webster et al., 2015

Figure 5.

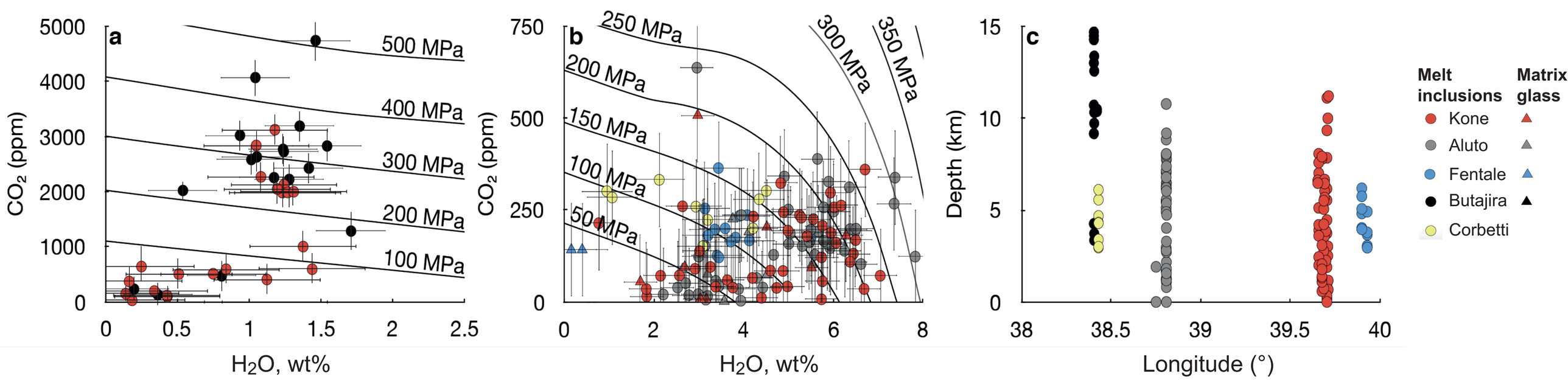
a
b
c
500 MPa
400 MPa
300 MPa
200 MPa
100 MPa
250 MPa
150 MPa
50 MPa
CO_2 (ppm)
H_2O, wt%
Depth (km)
Longitude (°)
Melt inclusions
Matrix glass
Kone
Aluto
Fentale
Butajira
Corbetti

Figure 6.

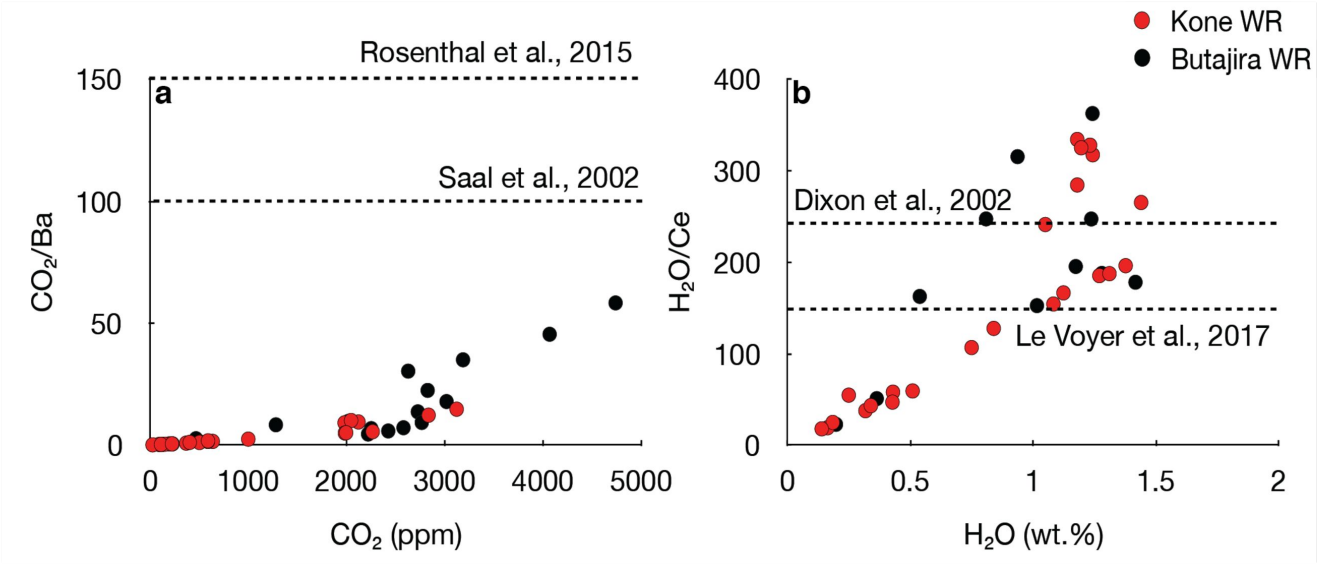
a
Rosenthal et al., 2015
Saal et al., 2002
150
100
50
0
CO_2/Ba
0
1000
2000
3000
4000
5000
CO_2 (ppm)
b
Kone WR
Butajira WR
Dixon et al., 2002
Le Voyer et al., 2017
400
300
200
100
0
H_2O/Ce
0
0.5
1
1.5
2
H_2O (wt.%)

Figure 7.

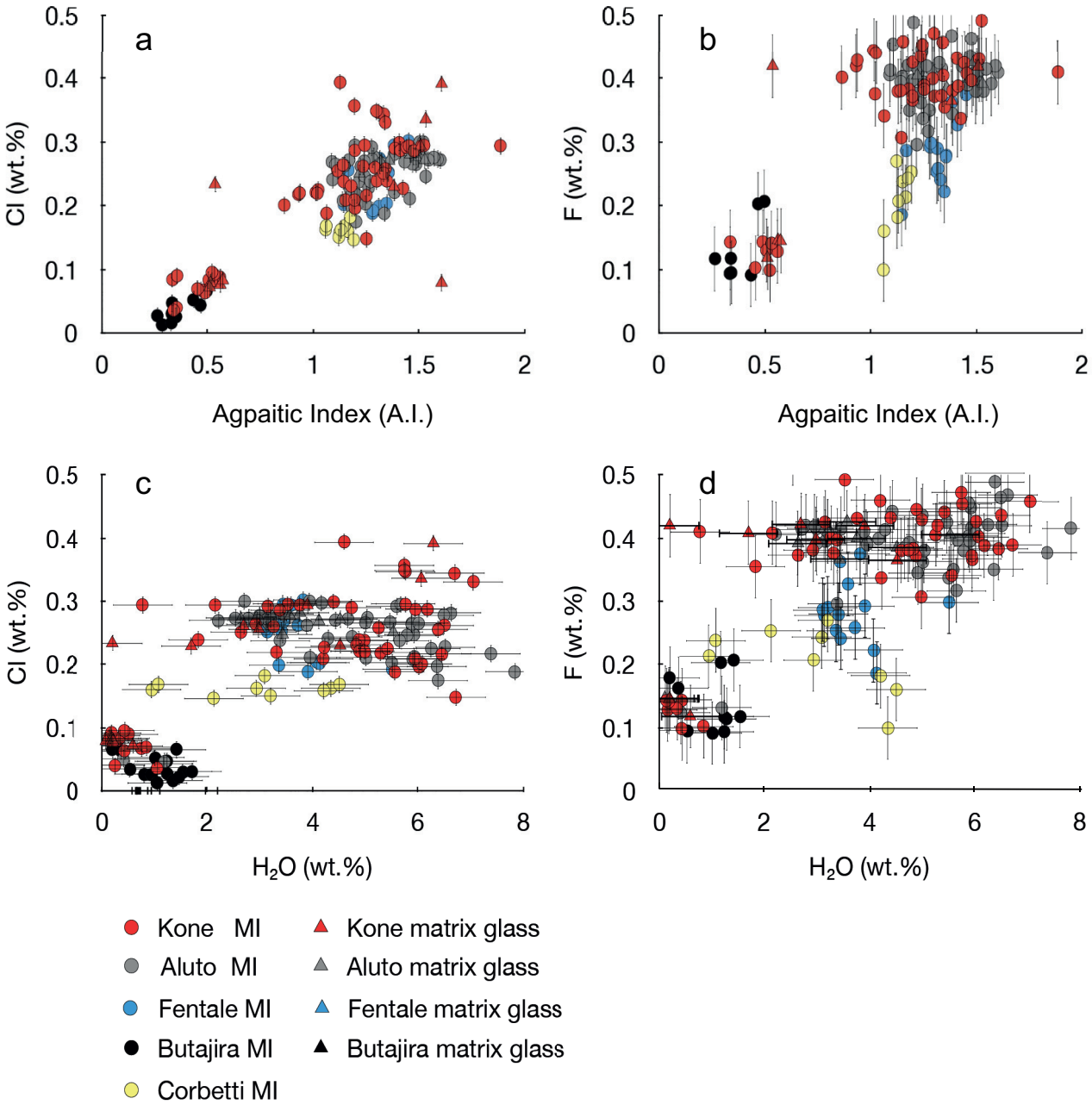
a
b
c
d
Cl (wt.%)
F (wt.%)
Agpaitic Index (A.I.)
H2O (wt.%)
0
0.1
0.2
0.3
0.4
0.5
0.5
1
1.5
2
2
4
6
8
Kone MI
Aluto MI
Fentale MI
Butajira MI
Corbetti MI
Kone matrix glass
Aluto matrix glass
Fentale matrix glass
Butajira matrix glass

Figure 8.

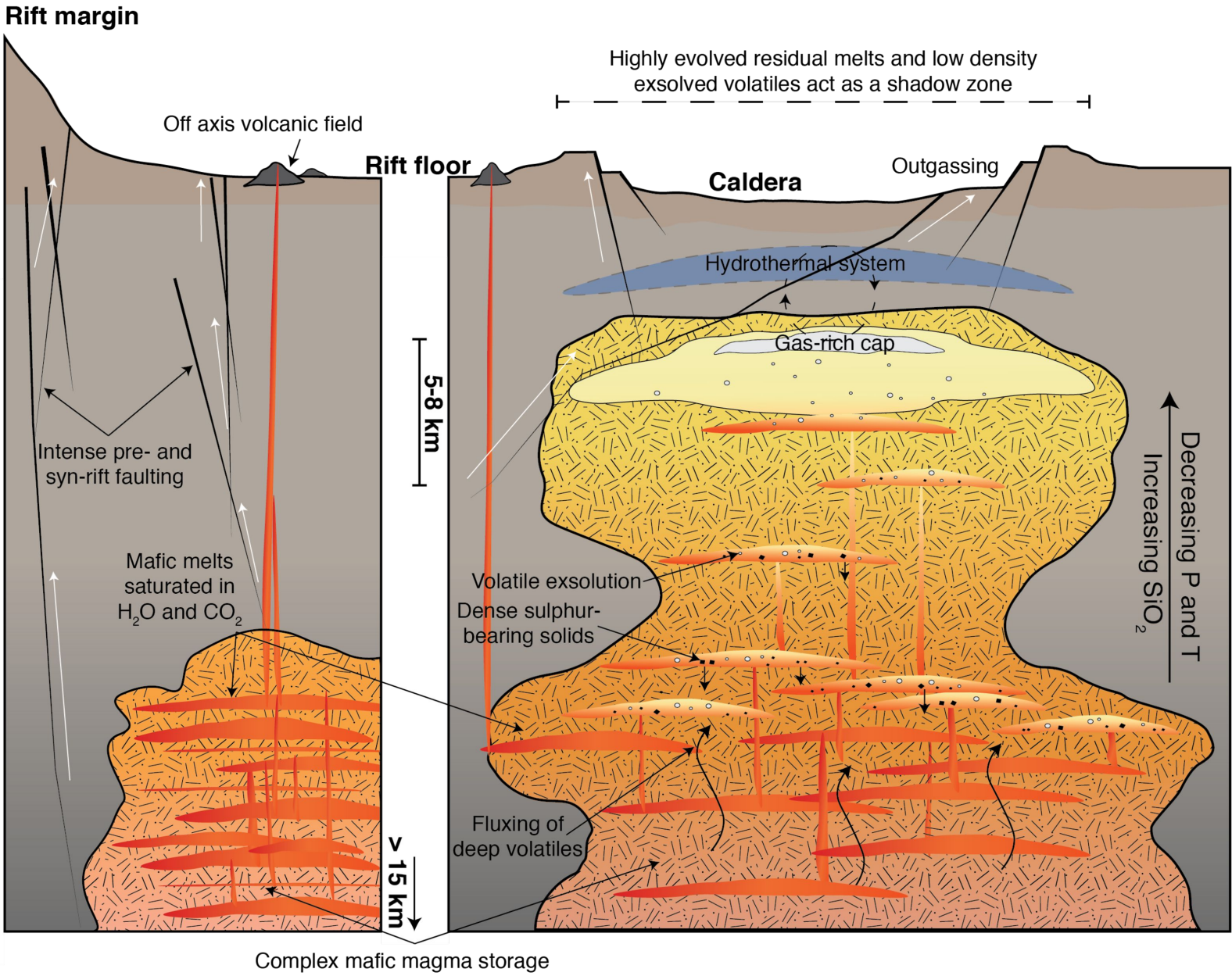
Rift margin
Highly evolved residual melts and low density exsolved volatiles act as a shadow zone
Off axis volcanic field
Rift floor
Caldera
Outgassing
Hydrothermal system
Gas-rich cap
5-8 km
Intense pre- and syn-rift faulting
Mafic melts saturated in H_2O and CO_2
Volatile exsolution
Dense sulphur-bearing solids
Decreasing P and T
Increasing SiO_2
Fluxing of deep volatiles
> 15 km
Complex mafic magma storage

Figure 9.

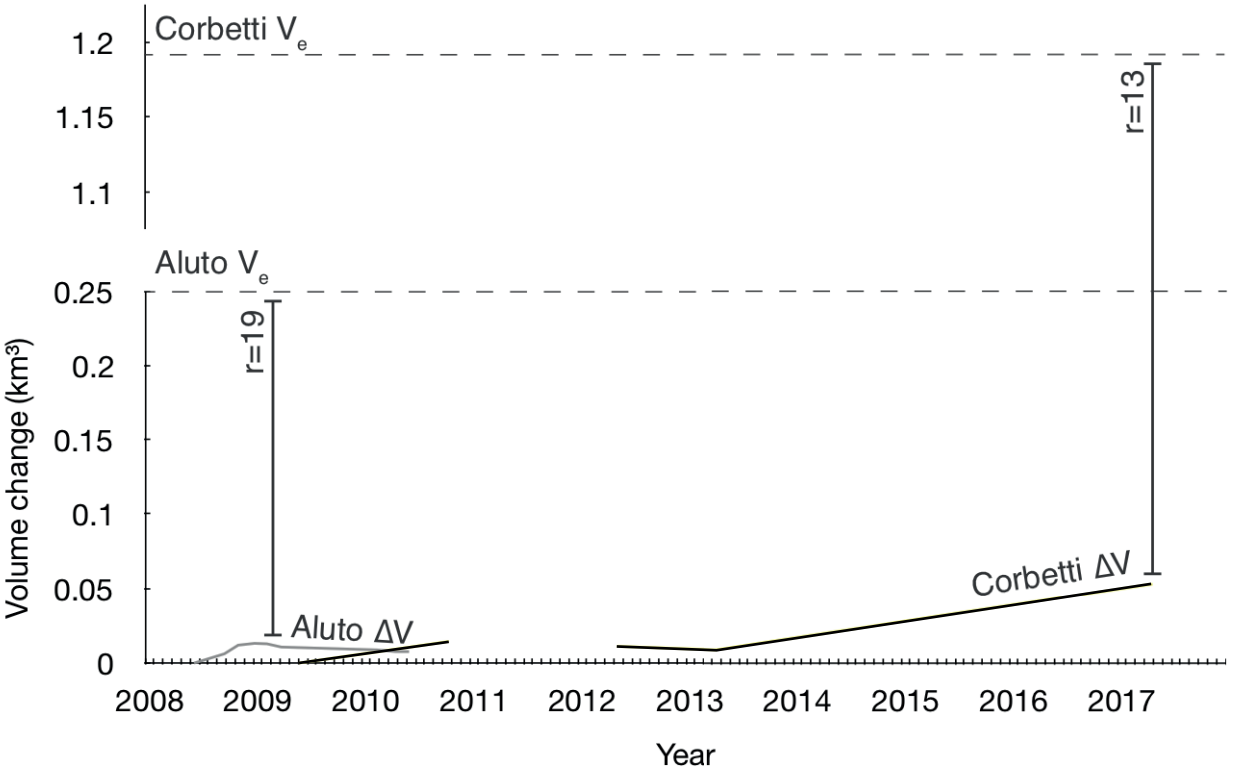
Corbetti V_e
Aluto V_e
r=13
r=19
Corbetti ΔV
Aluto ΔV
Volume change (km³)
Year
1.2
1.15
1.1
0.25
0.2
0.15
0.1
0.05
0
2008
2009
2010
2011
2012
2013
2014
2015
2016
2017